JOURNAL OF GEOPHYSICAL RESEARCH, VOL. 106, NO. D4, PAGES 3449–3474, FEBRUARY 27, 2001

A theoretical analysis of cloud condensation nucleus (CCN) instruments

Athanasios Nenes
California Institute of Technology, Pasadena, California

Patrick Y. Chuang
National Center for Atmospheric Research, Boulder, Colorado

Richard C. Flagan and John H. Seinfeld
California Institute of Technology, Pasadena, California

Abstract. The behavior and performance of four cloud condensation nucleus instruments are theoretically analyzed. They include the static diffusion cloud chamber (SDCC), the Fukuta continuous flow spectrometer (FCNS), the Hudson continuous flow spectrometer (HCNS), and the California Institute of Technology continuous flow spectrometer (CCNS). A numerical model of each instrument is constructed on the basis of a general fluid dynamics code coupled to an aerosol growth/activation model. Instrument performance is explored by simulating instrument response when sampling a monodisperse ammonium sulfate aerosol. The uncertainty in the wall temperature boundary condition is estimated for all the instruments and is found to be appreciable only for the CCNS. The CCNS and HCNS models reasonably reproduced experimental data, while reported limits were also verified by the FCNS model. Regarding the performance of each instrument, simulations show that the SDCC produces droplets that are monodisperse to within 10% of the particle diameter (for particles of a constant critical supersaturation). The FCNS can potentially activate particles over a wide range of critical supersaturations, but the prevailing design exhibits low sensitivity to particles with critical supersaturations below 0.1% as a result of the short time available for droplet growth under low supersaturations. The resolution capability of both HCNS and CCNS with respect to critical supersaturation is shown to be particularly sensitive to operational parameters. This is a consequence of the strongly nonlinear nature of droplet growth; droplet size cannot always be used to distinguish particles with different critical supersaturation because of the growing droplets' trend toward monodispersity. Of the two instruments, the HCNS generally displays higher resolution capability. This is attributed to the smoother and monotonic supersaturation profiles established in the HCNS. While different design parameters or operating conditions may lead to modest shifts in the performance from that predicted here for any of the four instruments, the essential features described in this paper are inherent to their designs.

1. Introduction

In theory, the cloud droplet activation spectrum of atmospheric aerosols can be inferred on the basis of composition. Measuring the complete chemical composition of atmospheric aerosol as a function of particle size in real time, however, is not yet possible. Therefore a direct measurement of the particles that activate to form droplets under supersaturations typical of atmospheric clouds is the accepted way to experimentally measure cloud condensation nuclei (CCN). Existing instruments to determine the CCN distribution expose an aerosol sample to a controlled environment with known water supersaturation profiles; the activation spectrum is then obtained by measuring the number (or size distribution) of particles that activate.

Paper number 2000JD900614.
0148-0227/01/2000JD900614$09.00

This study analyzes the performance of four existing CCN instrument designs. The main focus of this work is to determine the capability of each instrument (or, more precisely, of the methodology embodied by each instrument) to resolve a CCN activation spectrum. The resolution computed is solely a result of the process of CCN activation and growth within each instrument; uncertainty introduced by the droplet detection system is not considered. Furthermore, the models constructed here represent idealized instruments. This abstraction allows one to calculate the best possible (theoretical limit) resolution for an actual instrument; secondary effects not considered in these models will further degrade the resolution.

In addition to assuming idealized instruments, it is also assumed that a perfectly monodisperse aerosol is introduced, composed of pure $(NH_4)_2SO_4$. In reality, atmospheric aerosol is polydisperse and with a nonuniform composition. As a consequence, particles with the same potential for activation need different times for growth; this should have a deleterious effect on the instrument performance but will not be addressed in the current study.

An important uncertainty arises from the water film temperatures that are used to generate supersaturation in each instrument. Typically, CCN instruments measure and control temperatures by using thermocouples (or thermistors) that are embedded in the chamber wall rather than at the gas-wet surface interface. The actual temperature difference between the cold and hot water films is lower than the measured value owing to the thermal resistances of the plate and films, leading to a lower supersaturation than intended. As a result, the inferred activation spectrum is biased toward smaller sizes.

In the sections that follow, the CCN instruments are described; then the mathematical models used to simulate them are presented. An estimate of uncertainty in the water film temperature boundary conditions then follows. The response to a monodisperse aerosol input is simulated for each instrument. Finally, the performance of each (idealized) instrument is assessed on the basis of these simulations.

2. Description of CCN Instruments

Of the CCN instruments currently available, we will focus upon four: (1) the static diffusion cloud chamber (SDCC); (2) the continuous flow parallel plate chamber, specifically, the design of *Fukuta and Saxena* [1979] (FCNS); (3) the CCN spectrometer of *Hudson* [1989] (HCNS) and; (4) the California Institute of Technology (Caltech) CCN spectrometer (CCNS) [*Chuang et al.*, 2000]. Other instruments, for example, isothermal haze chambers (IHC) [*Laktionov*, 1972], have been used to measure CCN but will not be discussed here. IHC instruments do not actually activate the particles into droplets but rather measure the diameters of particles in equilibrium with an ambient relative humidity of 100%, from which the critical supersaturation, S_c, can be inferred. In theory, this is not a limitation if the particles are composed of inorganic salts, but ambiguity could arise if slightly soluble compounds or surfactants are present in the particles [*Alofs*, 1978; *Shulman et al.*, 1996].

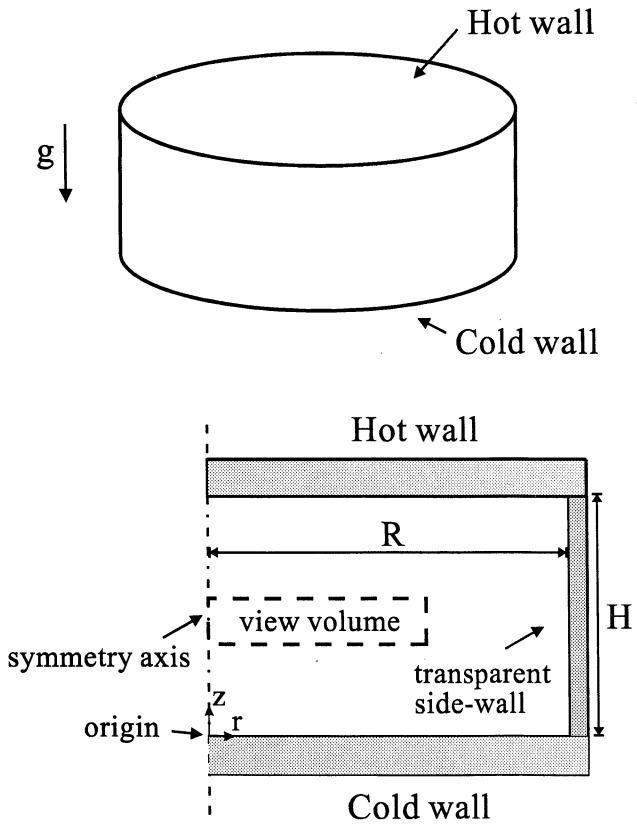

Figure 1. Static diffusion cloud chamber (SDCC).

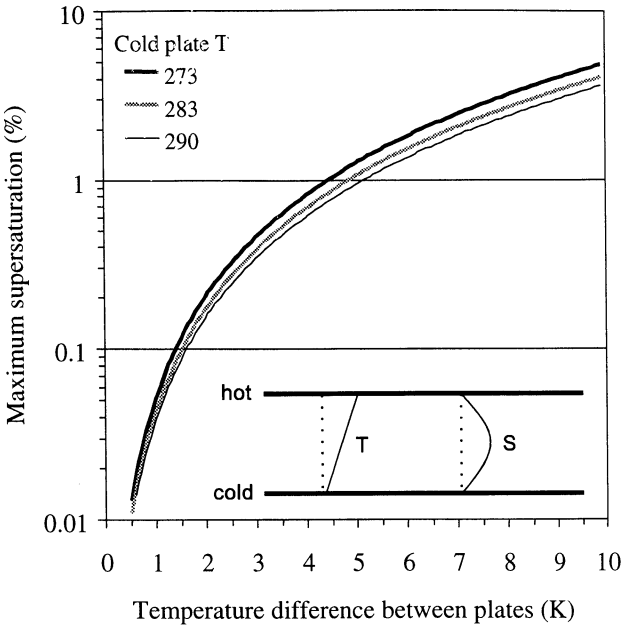

Figure 2. Maximum supersaturation (percent) in the SDCC as a function of hot and cold plate temperatures. Linear temperature and water vapor concentration profiles are assumed. Water vapor saturation pressure is calculated from a correlation given by *Seinfeld and Pandis* [1998].

2.1. Static Thermal Diffusion Cloud Chamber

These instruments are among the oldest for measuring CCN concentrations. The original static thermal diffusion chamber design [*Twomey*, 1963] consists of two parallel metal plates, held at different temperatures, with their facing surfaces wetted (Figure 1). Assuming quiescent conditions throughout the chamber, linear temperature and nearly parabolic supersaturation profiles develop between the plates, with the maximum supersaturation located midway. Figure 2 shows the maximum supersaturation generated in the SDCC for a variety of hot and cold plate temperatures. The CCN that are able to activate at the prescribed maximum supersaturation grow to become large droplets and in this way are distinguished from those that do not activate. The concentration of CCN that activate at this prescribed supersaturation is determined by measuring the droplet number concentration. In order to obtain the CCN spectrum, the number of activated droplets must be measured at several supersaturations, which is achieved by changing the temperature difference between the plates. This process typically requires several minutes per spectrum [*Lala and Jiusto*, 1977]. The lowest critical supersaturation that can be measured in the SDCC is around 0.2% [*Sinnarwalla and Alofs*, 1973].

One of the primary challenges regarding SDCC measurements involves the method used for counting the particles that activate within the region close to the maximum supersaturation. Initially, direct counting of the activated droplets was used but has been almost abandoned owing to the difficulty

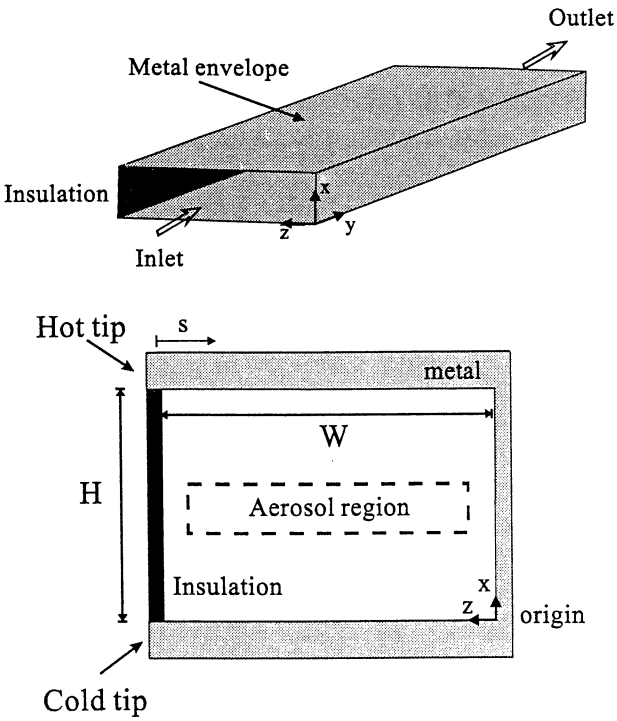

Figure 3. Fukuta continuous flow spectrometer (FCNS).

associated with such measurements. Photometric estimation is now the method of choice; concentration is inferred from the light scattered off the growing droplets contained within a view volume in the proximity of the instrument's center. Regardless of the scattering metric used (such as peak intensity, rate of signal growth, etc.), each introduces uncertainties that affect the resolution that can be obtained with SDCCs, because light scattering is a strong function of concentration and particle size (both of which vary considerably during the measurement).

One could make the simplifying assumption that all activating particles, regardless of their critical supersaturation, have approximately the same growth behavior. This approximation is reasonable when the critical supersaturation, S_c, is much smaller than the maximum supersaturation, S_{max} (because then the driving force for growth is approximately equal to the supersaturation). For S_c close to S_{max}, particles with different critical supersaturations need different times to grow up to a given size. Furthermore, the parabolic supersaturation profile within the instrument exposes particles to different supersaturations within the view volume; so droplets with the same critical supersaturation do not grow uniformly throughout the view volume. The combination of a nonuniform supersaturation profile and different growth rates among the activating particles generates a droplet distribution within the view volume that contributes to the uncertainty in the aerosol measurement. As was mentioned in the introduction, additional uncertainty could arise from the difference between the imposed and effective temperature differences.

2.2. Continuous Flow Parallel Plate Diffusion Chamber

The continuous flow parallel plate thermal diffusion chamber (CFDC) [*Sinnarwalla and Alofs,* 1973] was developed to overcome some of the limitations of the SDCC. Because the sample flow is continuous, the instrument operates at steady state, eliminating transients that complicate data analysis. Furthermore, useful data can be obtained continuously, rather than in the sampling intervals of batch cycle operation. When the sample is confined to the region close to the centerline of the instrument, all CCN are exposed to essentially the same supersaturation. CFDC measurements are limited to supersaturations larger than about 0.1%, owing to the long growth time required at low supersaturations. When the two plates are oriented horizontally, gravitational sedimentation limits the time during which droplets experience a uniform supersaturation and can cause significant particle loss within the instrument. For vertically oriented plates, the maximum temperature difference that can be imposed is limited by buoyancy-induced flows. Of the two configurations, however, the vertical seems to be more effective and is normally used.

An improvement of the CFDC was proposed by *Fukuta and Saxena* [1979] (FCNS). In this design, a gradient in temperature is imposed perpendicular to the flow direction, so that particles with the same residence time experience different supersaturations along different streamlines (Figure 3). This instrument therefore can be regarded as a series of CFDC instruments operating simultaneously at different temperature differences. Figure 4 shows qualitative temperature and supersaturation profiles perpendicular to the flow for fully devel-

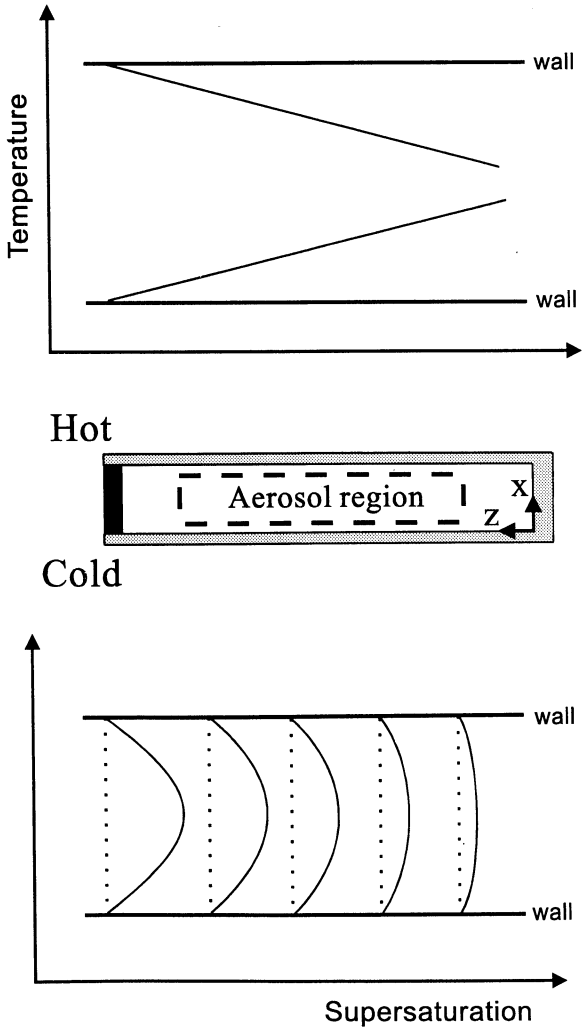

Figure 4. Typical temperature and supersaturation profiles for the FCNS along a flow section, for developed inlet conditions.

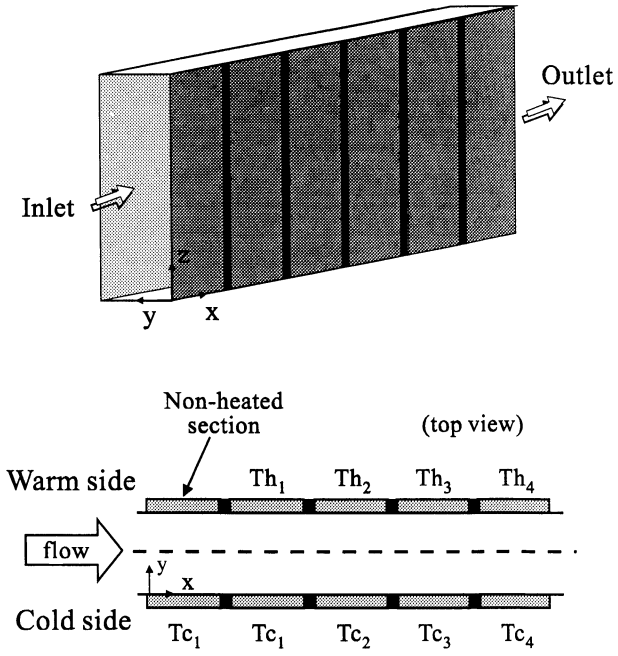

Figure 5. Hudson continuous flow spectrometer (HCNS).

oped laminar flow (neglecting sidewall and buoyancy effects). The profiles for a given streamline are similar to those attained in the SDCC at steady state; so diagrams such as Figure 2 can be used for predicting S_{max} at different positions in the instrument. It should be noted that S_{max} is attained toward the exit of the instrument, after the concentration and temperature fields develop. A significant portion of the instrument is used to "precondition" the aerosol flow, by developing the velocity and temperature profiles before exposing the flow to the wetted hot wall. If this is not done, incoming air that mixes with saturated hot air in the entrance region of the instrument can generate much higher supersaturations than intended. This may bias the measurement by activating aerosol corresponding to a different supersaturation than prescribed. Strictly speaking, the FCNS is a particle counter, since each streamline is exposed to only one supersaturation (after the flow completely develops). If all streamlines are simultaneously probed, a CCN spectrum can be obtained in real time.

2.3. Dynamic CCN Spectrometers

The underlying idea behind these instruments is to expose an aerosol sample to a variable supersaturation field and infer the CCN spectrum from the outlet droplet size distribution. CCN with low S_c are expected to activate near the entrance of the instrument, and so they have more time to grow than do particles with higher S_c; the latter activate farther down the instrument. Therefore the outlet droplet size is expected to decrease with increasing critical supersaturation. Furthermore, the initial size of the particles entering the instrument (being in equilibrium with the inlet RH) decreases with increasing critical supersaturation, thus enhancing the size differences between particles of different critical supersaturation, S_c. The sensitivity of the instrument depends critically on how the outlet droplet size varies with particle dry size, and hence S_c. Because the rate of droplet growth varies inversely with particle diameter, the droplet size distribution considerably narrows as particles grow, implying that a very precise size measurement may be needed at the outlet of the instrument. Compared with SDCCs and CFDCs, dynamic spectrometers utilize a completely different concept in instrument design, in both the activation and size measurement components.

Hudson [1989] developed a dynamic spectrometer by modifying a continuous flow thermal diffusion chamber (HCNS) (Figure 5). This instrument exposes the sample air to a supersaturation profile that increases in the streamwise direction, as shown in Plate 1. The flow field is preconditioned before a supersaturation is imposed, in a similar fashion to the FCNS. Because the HCNS design measures particles over a large range of S_c simultaneously, CCN spectra can potentially be determined rapidly. The reported range of measurable critical supersaturations in the HCNS is considerably larger than that for thermal diffusion chambers, 0.01 to 1%, covering much of the range of interest for climatically important warm clouds. The supersaturation range is extended because low S_c particles are exposed to very high supersaturations, thus considerably accelerating their growth. This instrument also uses white light size detection, eliminating any size ambiguity from Mie scattering resonances seen in laser size detection. Because

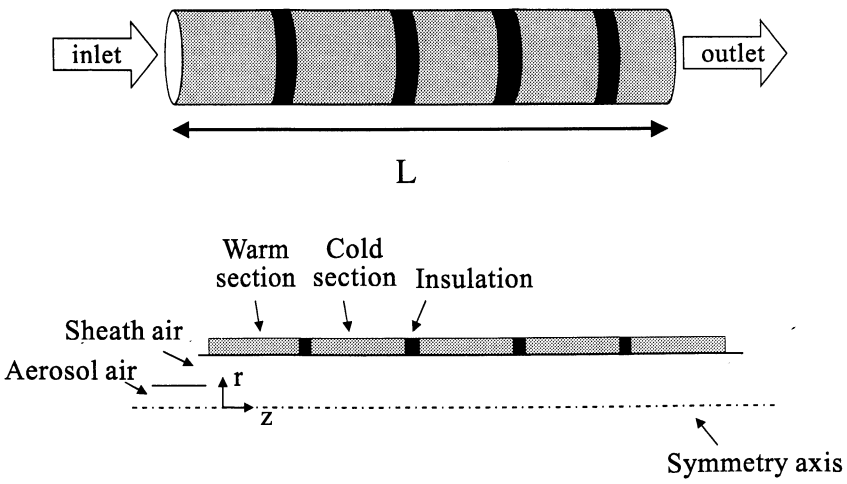

Figure 6. Caltech continuous flow spectrometer (CCNS).

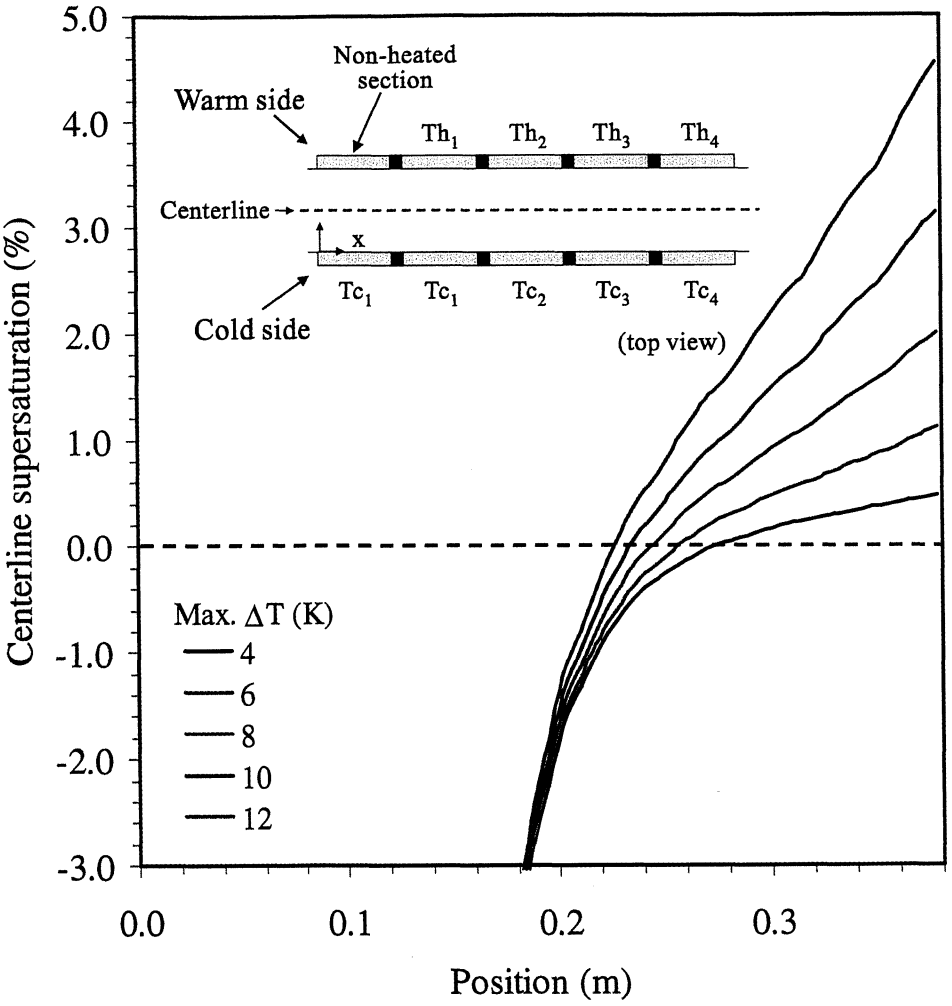

Plate 1. Typical supersaturation (percent) profiles for the HCNS along a flow section, for various maximum temperature differences, ΔT_{max} (the ΔT at the last segment). The temperature difference between each segment is assumed to increase with a constant step ("linear ramp") on both cold and warm sides. The profiles are computed by using the HCNS numerical model in this paper.

of the speed and wide range of supersaturations that can be covered, this instrument has been used frequently on airborne measurements [*McMurry*, 2000].

The Caltech CCN spectrometer (CCNS) [*Chuang et al.*, 2000] (Figure 6) implements Hudson's streamwise gradient method in tube flow. A method originally developed by *Hoppel et al.* [1979] is employed to produce supersaturation in the flow in a wet-walled cylindrical tube; the tube is divided along its length into sections that are alternately heated or cooled. As the air flows through the tube, it is saturated in the warm sections and then cooled to produce supersaturation near the center of the tube. The supersaturation profile that develops depends on the geometry of the segments, the flow rates, the temperature difference, and the operating pressure. The supersaturation is increased along the length of the tube by increasing the temperature difference between successive tube segments, leading to a centerline supersaturation profile such as that shown in Figure 7. The first section can be used to precondition the inlet flow.

Another important issue is to estimate the uncertainty that would arise when calibration curves produced by using pure salt aerosol are used to infer ambient CCN spectra. Both spectrometers operate on the assumption that particles with the same S_c (but different composition) will have the same growth behavior when exposed to an identical supersaturation field. In reality, an even stricter constraint must be satisfied: the Köhler curves need to be similar, which is not the case for aerosol-containing surfactant and slightly soluble material. Furthermore, the inlet air may also contain condensable gases that can also have a large impact on the activation properties of the aerosol; this may not be correctly accounted for in the instrument. These issues are to be addressed in future studies.

3. Mathematical Models of CCN Instruments

To evaluate the performance of the different CCN instruments, flow, heat, and mass transfer have been numerically modeled within each instrument to determine the temperature, water vapor, and supersaturation distributions as a function of position and, for unsteady instrument operation, time. Particle activation and growth are simultaneously simulated by tracking individual particles as they flow through the instrument.

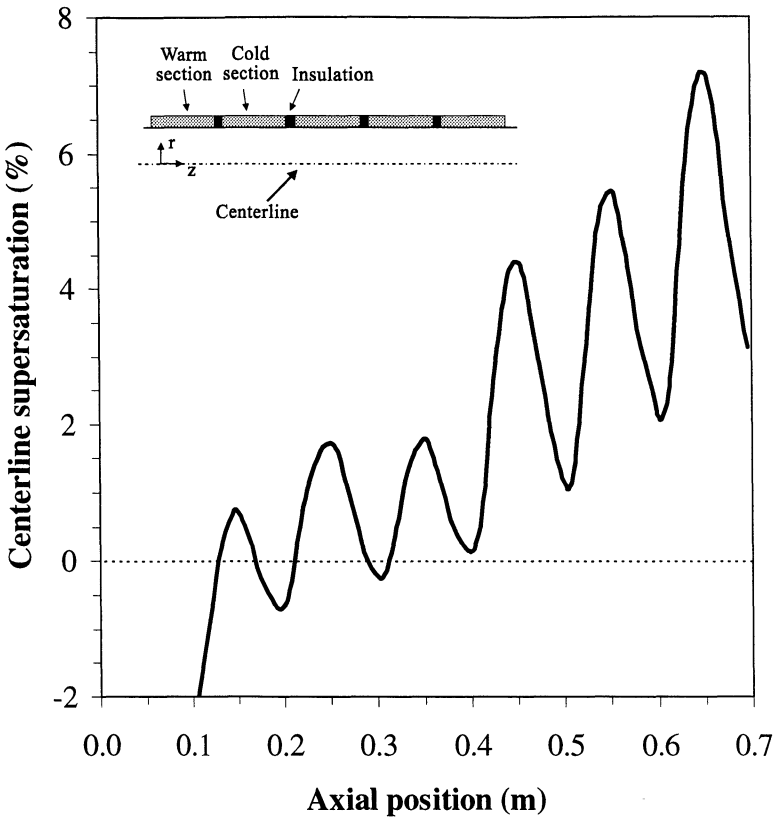

Figure 7. Indicative supersaturation (percent) profile for the CCNS along a flow section. The volumetric flow rate is 0.7 L min^{-1}. The profile is computed by using the CCNS numerical model of this paper.

The equations used to describe aerosol particle growth are first given in the next section, followed by the general form of the gas phase equations used for all the instruments. Finally, the appropriate boundary conditions and specific relations for each instrument are given.

3.1. Aerosol Growth

The rate of change of droplet size for each of the particles is calculated from the diffusional growth equation [*Seinfeld and Pandis,* 1998]:

$$D_p \frac{dD_p}{dt} = \frac{S_v - S_v^{eq}}{\dfrac{\rho_w RT}{4p^* D_v' M_w} + \dfrac{\Delta H_{vap}\rho_w}{4k_a' T}\left(\dfrac{\Delta H_{vap} M_w}{TR} - 1\right)}, \quad (1)$$

where D_p is the particle diameter, p^* is the saturation vapor pressure at the local temperature T, $S_v = p_v/p^* - 1$ is the local supersaturation, S_v^{eq} is the equilibrium supersaturation of the droplet, ρ_w is the water density, ΔH_{vap} is the enthalpy of vaporization of water, M_w is the molar mass of water, and R is the universal gas constant. D_v' is the diffusivity of water vapor in air modified for noncontinuum effects [*Fukuta and Walter,* 1970]:

$$D_v' = \frac{D_v}{1 + \dfrac{2D_v}{a_c D_p}\sqrt{\dfrac{2\pi M_w}{RT}}},$$

where D_v is the diffusivity of water vapor in air, a_c is the condensation coefficient. The thermal conductivity of air modified for noncontinuum effects, k_a' is given by

$$k_a' = \frac{k_a}{1 + \dfrac{2k_a}{a_T D_p \rho c_p}\sqrt{\dfrac{2\pi M_a}{RT}}},$$

where M_a is the mean molar mass of air, k_a is the thermal conductivity of air, ρ is the air density, c_p is the heat capacity of air, and a_T is the thermal accommodation coefficient. The equilibrium supersaturation of the droplet, S_v^{eq} is given by the Köhler equation:

$$S_v^{eq} = \exp\left[\frac{4M_w\sigma_w}{RT\rho_w D_p} - \frac{6n_s M_w \nu_s}{\pi\rho_w\left(D_p^3 - d_p^3\right)}\right] - 1,$$

where σ_w is water surface tension, n_s is the number of moles of solute per particle, and d_p is the dry diameter of the particle.

3.2. Gas Phase Equations

Differential momentum, energy, and mass conservation balances are written for the gas phase, assuming a two-dimensional Cartesian or axisymmetric coordinate system. This results in a system of differential equations, each of which is of the general form

$$\frac{\partial}{\partial t}\left(x_2^a \rho\phi\right)+\frac{\partial}{\partial x_1}\left(x_2^a \rho u\phi\right)+\frac{\partial}{\partial x_2}\left(x_2^a \rho v\phi\right) - \frac{\partial}{\partial x_1}\left(x_2^a \Gamma_\phi \frac{\partial\phi}{\partial x_1}\right)-\frac{\partial}{\partial x_2}\left(x_2^a \Gamma_\phi \frac{\partial\phi}{\partial x_2}\right)=S_\phi, \quad (2)$$

where x_1, x_2 are the spatial coordinates and ϕ is the dependent variable (e.g., T). S_ϕ is a source term, and Γ_ϕ is a transport coefficient, both of which depend on the form of ϕ. Table 1 lists the expressions of S_ϕ, Γ_ϕ for each type of ϕ. For Cartesian geometry, the exponent $a = 0$ and the coordinates x_1, x_2 can be replaced with the more conventional x, y. For axisymmetric geometry, $a = 1$ and the coordinates x_1, x_2 can be replaced with the more conventional z, r.

The rate of condensation of liquid water (in moles per volume of air per second) on the aerosol particles, J_{cond}, is needed in the water vapor and energy conservation equations. This quantity is given by

$$J_{\text{cond}} = \frac{1}{M_w}\frac{dw_L}{dt},$$

where w_L is the local liquid water content (kg m^{-3} air). For a population of water droplets consisting of N_i droplets of diameter D_{pi} per volume of air,

$$w_L \approx \rho_w \frac{\pi}{6}\sum_{i=1}^{n} N_i D_{pi}^3,$$

where n is the number of droplet sizes found in the distribution and ρ_w is the density of water. On the basis of this definition of w_L, the rate of change of liquid water content of the particles is

$$\frac{dw_L}{dt} = \frac{d}{dt}\left\{\rho_w \frac{\pi}{6}\sum_{i=1}^{n} N_i D_{pi}^3\right\} = \rho_w \frac{\pi}{2}\sum_{i=1}^{n} N_i D_{pi}^2 \frac{dD_{pi}}{dt}, \quad (3)$$

where dD_{pi}/dt is calculated from the aerosol growth equations. Substituting equation (3) into the definition for J_{cond} gives

$$J_{\text{cond}} = \frac{\pi}{2}\frac{\rho_w}{M_w}\sum_{i=1}^{n} N_i D_{pi}^2 \frac{dD_{pi}}{dt}. \quad (4)$$

Furthermore, a source term in the momentum equations, J_{buoy}, represents the momentum generated from thermal buoyancy effects. For ideal gases it is given by

$$J_{\text{buoy}} = -\rho g_{x_2}\left[\frac{T - T_{\text{bulk}}(x_2)}{T_{\text{bulk}}(x_2)}\right], \quad (5)$$

where T is the temperature and g_{x_2} is the component of gravity in the x_2 direction. $T_{\text{bulk}}(x_2)$ is the x_1 average temperature at position x_2 and is computed differently for each instrument. Finally, ρ is gas phase density, calculated at $T_{\text{bulk}}(x_2)$.

3.3. Static Diffusion Cloud Chamber

The geometry and characteristic parameters of the SDCC are shown in Figure 1. The following assumptions are made to simulate the instrument: (1) there is a two-dimensional axisymmetric chamber geometry; (2) the air is quiescent; (3) particles fall by gravitational sedimentation and attain terminal velocity instantaneously as they grow; (4) coagulation and Brownian diffusion of particles are neglected; and (5) wet walls act as a perfect sink/source of water vapor, *i.e.,* the air is saturated with water vapor at the walls.

At the top and bottom walls, a constant temperature boundary condition is imposed, while at the symmetry axis, $\partial T/\partial r = 0$. At the sidewall, a composite heat conduction-natural convection heat flux boundary condition is used,

$$\dot{q} = U(T_{\text{amb}} - T_f), \quad (6)$$

where $\dot{q}$ is the heat flux per unit area, T_{amb} is the ambient temperature outside of the cell, T_f is the air temperature at the computational cell adjacent to the sidewall, and U is the appropriate heat transfer coefficient between the outside ambient and chamber fluid,

$$\frac{1}{U} = \frac{C_p}{h} + \frac{C_p}{k_{\text{wall}}}\ln\left(1+\frac{\Delta r}{R}\right), \quad (7a)$$

where C_p is the wall heat capacity, k_{wall} is the sidewall thermal conductivity, and h is the natural convection heat transfer coefficient, calculated by the following correlation [*Incropera and DeWitt*, 1985]:

Table 1. Transfer Coefficients and Source Terms for the Gas Phase Equations

Conservation Law	ϕ	Γ_ϕ	S_ϕ
Continuity	1	0	0
x_1 momentum	u	μ	$-x_2^a\frac{\partial P}{\partial x_2}+x_2^a\frac{\partial}{\partial x_1}\left(\mu\frac{\partial u}{\partial x_2}\right)+\frac{\partial}{\partial x_2}\left(x_2^a\mu\frac{\partial v}{\partial x_2}\right)+J_{\text{buoy}}$
x_2 momentum	v	μ	$-x_2^a\frac{\partial P}{\partial x_2}+x_2^a\frac{\partial}{\partial x_1}\left(\mu\frac{\partial u}{\partial x_2}\right)+\frac{\partial}{\partial x_2}\left(x_2^a\mu\frac{\partial v}{\partial x_2}\right)-\frac{a\mu v}{x_2}$
Heat	T	$\frac{k_a}{c_p}$	$\frac{\Delta H_{\text{vap}}}{c_p}J_{\text{cond}}$
Water vapor	C	ρD_v	$-\rho J_{\text{cond}}$

$$\frac{hL}{k_a} = Nu_L = 0.68 + \frac{0.670 Ra_L^{1/4}}{\left[1+(0.492/\mathrm{Pr})^{9/16}\right]^{4/9}}, \qquad (7b)$$

where

$$Ra = \frac{c_p \rho^2 g L^3}{\mu k_a} \frac{\bar{T}_w - T_{amb}}{T_{amb}}$$

is the Rayleigh number for an ideal gas, $Pr = \mu/\rho k_a$ is the Prandtl number, $\bar{T}_w$ is the average temperature of the SDCC Plexiglas wall, and T_{amb} is the ambient temperature. The first term on the right-hand side of equation (7a) is the heat conduction resistance between the outer sidewall and the environment, and the second term is the resistance within the sidewall. At the sidewall and the symmetry axis, $\partial C/\partial r = 0$. Particles are assumed initially to occupy the entire chamber, with a uniform concentration and size distribution throughout.

The droplet sedimentation velocity is given by the Stokes equation [*Seinfeld and Pandis*, 1998],

$$u_t = \frac{D_p^2 \rho_p g C_c}{18\mu}, \qquad (8)$$

where

$$C_c = 1 + (2\lambda/D_p)\left[1.257 + 0.4\exp(-1.1 D_p/\lambda)\right]$$

is the slip correction factor, ρ_p is the particle density, μ is the air viscosity, g is the gravity constant, and λ is the mean free path of air.

3.4. Fukuta Continuous Flow Spectrometer

Using scaling arguments, it can be shown that sidewall effects in the velocity field become significant when the distance from the sidewalls is of order H. The FCNS geometry examined has an aspect ratio of $W/H = 20$; so more than 90% of the total width of the instrument remains unaffected by the presence of walls. Thus the FCNS (Figure 3) can be reasonably simulated by solving a series of two-dimensional problems, each of which is for a fixed value of the z coordinate. A vertical flow configuration is assumed. In addition, the following assumptions are made: (1) conditions are steady state; (2) aerosol particles follow the air flow streamlines, at the same velocity as the surrounding air; (3) coagulation and Brownian diffusion of particles are neglected; (4) walls act as a perfect sink/source of water vapor; and (5) the temperature profile along the wall (in the z direction) is linear.

Two types of inlet velocity conditions are considered, fully developed (i.e., parabolic) or plug flow. The other variables (T, C) are assumed to have a uniform profile at the inlet. At the walls, a no-slip boundary condition is assumed, $u = v = 0$, and for the outlet, $\partial u/\partial x = 0$; $v = 0$. At the outlet, $\partial T/\partial x = 0$. A constant temperature condition is used for the walls; this is a function of the z position of the section examined and is computed by using assumption (5). Given that the temperature at the two tips T_h (for any x, $y = H$ and $z = W$) and T_c (for any x, $y = 0$ and $z = W$) are known, the temperatures at the top wall T_t and the bottom wall T_b at a given coordinate z are

$$T_t(z) = T_h - \left(\frac{dT}{ds}\right)(W - z) \;;\; T_b(z) = T_c + \left(\frac{dT}{ds}\right)(W - z),$$

where s is a coordinate that runs along the heated wall, with its origin located at the hot tip (Figure 3) and ends at the cold tip;

$$\frac{dT}{ds} = \frac{T_h - T_c}{2W + H}$$

is the temperature gradient along the s coordinate. At the walls, the air is assumed to be saturated with water vapor at the local temperature. At the outlet, $\partial C/\partial x = 0$. Based on the sheath/aerosol flow ratio, the section of the flow field occupied by the aerosol is calculated from a mass balance. Finally, the mean temperature

$$T_{bulk}(y) = \frac{\int_0^H T(x,y)dx}{\int_0^H dx}$$

is used in calculating the buoyancy term in the u momentum equation.

3.5. Hudson Continuous Flow Spectrometer

In simulating the HCNS (Figure 5), the following assumptions are invoked: (1) conditions are steady state; (2) geometry is two-dimensional Cartesian; (3) aerosol particles follow the air flow streamlines with the same velocity as the surrounding air; (4) sedimentation, coagulation, and Brownian diffusion of particles are neglected; (5) walls act as a perfect sink/source of water vapor, i.e., the air is saturated with water vapor right adjacent to the walls; and (6) buoyancy is neglected. The two-dimensional assumption neglects top and bottom wall effects. This can be shown through scaling arguments to be a good approximation when the aspect ratio H/W is large and breaks down only when the distance from the sidewalls is of order W. In addition to the constant temperature condition posed at the controlled temperature sections, a zero-heat flux condition is assumed at the insulated areas.

3.6. Caltech Continuous Flow Spectrometer

In formulating the conservation equations for the CCNS, the same assumptions as those for the HCNS are made, except that an axisymmetric coordinate system is used. Although buoyancy is not expected to be significant, it is included in the model for completeness. $T_{bulk}(z)$ in this case is the radial-average temperature at axial position z:

$$T_{bulk}(z) = \frac{\int_0^R 2\pi r T(r,z)dr}{\int_0^R 2\pi r dr}.$$

Boundary inlet conditions used are similar to those of section 3.4. In addition to those, $\partial u/\partial r = \partial v/\partial r = \partial C/\partial r = \partial T/\partial r = 0$ at the symmetry axis.

4. Numerical Solution of Conservation Equations

The conservation equations for the four instruments cannot be solved analytically; so a numerical solution is obtained by the finite volume method [*Patankar*, 1980]. A hybrid upwind-central differencing scheme is used for calculating the convective-diffusive fluxes over the finite control volumes. The scheme used employs a staggered grid, in which each velocity grid node lies between two scalar volumes, ensuring that the numerical solution is consistent with respect to pressure. The Semi-Implicit Method for Pressure-Linked Equations (SIMPLE) iterative solution method [*Patankar*, 1980] is used to solve the hydrodynamic cycle of the finite volume equations, while the particle growth equations are solved numerically integrated with the LSODE solver of *Hindmarsh* [1983]. The computer code used for the numerical simulations was based on the TEACH-2E CFD code [*Gosman and Ideriah*, 1976] coupled together with an aerosol growth module. The computational grid and time step used ensure that the numerical solution is within a few percent of the asymptotic (with respect to grid density) limit. The numerical solution was obtained by using 100 cells for each spatial coordinate. For the unsteady state simulations of the SDCC, a time step of 0.025 s is taken for the gas phase equations, for a total integration time of 30 s. The aerosol growth equations use a variable time step, which is scaled depending on the instrument simulated. For the SDCC simulations, it is scaled on the gas phase time step, while the others use the transit time through a computational cell.

5. Uncertainty Analysis for Wall Temperature of CCN Instruments

Before proceeding with the numerical simulation of the instruments, it is instructive to perform an analysis of the uncertainty in one of the most critical parameters of CCN instruments, namely, the temperature boundary condition for the instrument wall. When operating the instruments, one controls the temperature of the metal supporting wall (or plates), whereas the boundary condition that actually governs the performance of the instrument is the temperature of the inner face of the water film on the wall. Differences between these two temperatures would bias the predictions, since the supersaturation is a strong function of temperature difference. One could include heat transfer through the walls and film in the simulations, but the analysis of constant wall temperature is adequate for the purpose of estimating the relative magnitude of the uncertainty arising from a temperature difference. Furthermore, such an analysis is useful in that it is independent of any specific geometry or configuration.

When estimating the wall temperature uncertainty, one must consider all the factors that contribute to the temperature drop between the controlled temperature side and the water film. Apart from the metal walls and the water film, there is also a material that helps keep the walls wet. The material conventionally used for the SDCC, FCNS, and CCNS is filter paper, while the HCNS uses a steel matrix. The material will be shown to have a larger impact on the wall temperature uncertainty in the continuous flow instruments than on the SDCC. The results for the SDCC may be considered intuitive, but the analysis is included for completeness.

In order to assess the effect of wall temperature uncertainty, simple heat transfer models will be constructed for all of the instruments. In these models, the inner water film temperature, T_f, is estimated from the heat flux through the walls. The temperature difference between T_f and the controlled wall temperature, T_w, is then computed and expressed as a fraction of the "nominal" difference, $T_h - T_c$, for various values of water film thickness, filter paper thickness, and flow rates. Realistic values for both paper and water film thickness are 10^{-3} m; the wall is assumed to be of order 10^{-2} m.

5.1. SDCC Uncertainty Analysis

With respect to wall heat transfer in the SDCC, the following can be assumed: (1) steady state conditions and (2) one-dimensional conductive heat transfer (stagnant flow field) along the axial direction of the instrument (see Figure 8a). With these assumptions, the heat flux between points 1 and 2, $Q_{1,2}$, is equal to the heat flux between the top and bottom wall, $Q_{t,b}$. Expressing these fluxes as a function of the temperature differences, $T_h - T_c$ and $T_1 - T_2$, we have $Q_{1,2} = Q_{t,b}$, which leads to

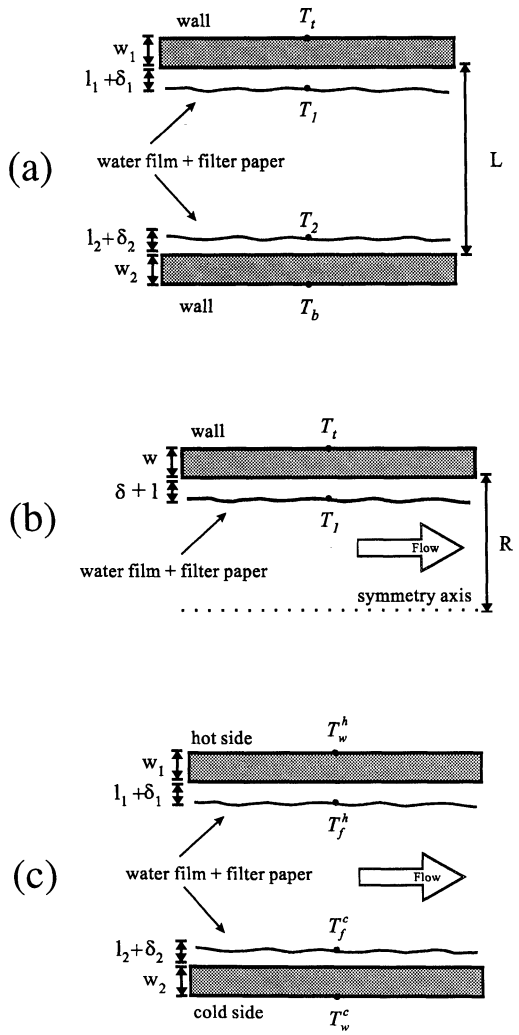

Figure 8. Geometries used in the simple models developed for determining the uncertainty in the temperature boundary conditions for (a) the SDCC; (b) the CCNS, and (c) the HCNS.

$$U_{1,2}(T_1 - T_2) = U_{t,b}(T_h - T_c), \tag{9}$$

where $U_{1,2}$ and $U_{t,b}$ are the total heat transfer coefficients between points 1, 2 and t, b, respectively. These heat transfer coefficients can be evaluated by the resistance method [*Incropera and DeWitt*, 1985] to lead to

$$\frac{1}{U_{1,2}} = \frac{L - (l_1 + l_2) - (\delta_1 + \delta_2)}{k_a} \tag{10}$$

$$\frac{1}{U_{t,b}} = \frac{(w_1 + w_2)}{k_{\text{st.steel}}} + \frac{L - (l_1 + l_2) - (\delta_1 + \delta_2)}{k_a} + R_{s1} + R_{s2}, \tag{11a}$$

where $k_{\text{st.steel}} = 15$, $k_{\text{water}} = 0.58$ and $k_{\text{paper}} = 0.1$ are the thermal conductivities (in W m^{-1} K^{-1}) of stainless steel, water, and filter paper, respectively. Also, w_i, l_i, and δ_i are the thickness of the wall, filter paper, and water film, respectively (i = 1 corresponds to the hot plate, while i = 2 refers to the cold plate). In equation (11a), the resistances of the wall, soaked filter paper, and air are assumed to be in series. The resistance of the soaked filter paper, R_{si}, is

$$R_{si} = \frac{1}{\dfrac{k_{\text{water}}}{\min(\delta_i, l_i)} + \dfrac{k_{\text{paper}}}{\min(\delta_i, l_i)}} + \frac{\delta_i - \min(\delta_i, l_i)}{k_{\text{water}}} + \frac{l_i - \min(\delta_i, l_i)}{k_{\text{paper}}}. \tag{11b}$$

The first term in the above equation assumes that an equal segment of water and filter paper are combined in parallel (which corresponds to the well-soaked portion of the filter paper), and the remaining paper (or water) is connected in series. Allowing for the excess of filter paper and water considers situations where the filter paper is partially dry or when too much water is provided on the filter paper. The sensitivity of the uncertainty to these conditions is an important operating parameter of these instruments.

Substituting equations (11a), (11b), and (10) into (9) and solving for $(T_1 - T_2)/(T_h - T_c)$ yield

$$\frac{T_1 - T_2}{T_h - T_c} = \left(1 + \frac{(w_1 + w_2)\dfrac{k_a}{k_{\text{st.steel}}} + R_{s1}k_a + R_{s1}k_a}{L - (l_1 + l_2) - (\delta_1 + \delta_2)} \right)^{-1}. \tag{12}$$

The uncertainty could therefore be defined as

$$\left(1 - \frac{T_1 - T_2}{T_h - T_c} \right) \times 100\%.$$

Using equation (12), we calculate that for cases where the water and paper thicknesses are equal, the ratio is at most 0.99. This means that the effective temperature difference is practically equal to the nominal. For example, for $T_h - T_c = 2\ K$, then, depending on the thickness of the water film, $T_1 - T_2$ is about 1.99 K, the uncertainty thus being at most 0.01 K. This result is not surprising, since the gap between the plates is occupied mostly by air, which has low thermal conductivity compared with conductivities of the other materials. The resistance therefore to heat conduction is mainly owing to the air and is relatively insensitive to the presence of water and filter paper. In addition, variations in water film or changes in wall thickness do not have a large impact on the uncertainty. It can be concluded that once the steady state temperature profile has been achieved, the temperature uncertainty in the instrument is negligible.

5.2. CCNS Uncertainty Analysis

In our presentation of the two spectrometers, usually the HCNS precedes the CCNS. For convenience, however, we shall begin now with the CCNS, for which we assume the following: (1) conditions are steady state; (2) there is one-dimensional conductive heat transfer along the radial direction and convective heat transfer along the axial direction of the instrument; (3) on the entry to each hot and cold segment, the temperature profile is uniform and equal to the wall temperature of the previous section; (4) the flow field is fully developed and laminar; and (5) the latent heat flux from water condensation through the wall is small in comparison with the sensible heat transfer, which is reasonable for near–atmospheric pressures and small temperature differences. The appropriate geometry is defined in Figure 8b. With these assumptions, the problem reduces to a developing temperature profile in the entry region of a pipe, with a fully developed hydrodynamic flow field. The heat flux through the wall for the given segment therefore can be calculated by

$$\dot{q} = hA\Delta T, \tag{13}$$

where A is the total surface exchange area, ΔT is the temperature change of the bulk fluid between entry and exit of the pipe segment, and h is the mean heat transfer coefficient, which is calculated by the following correlation [*Incropera and DeWitt*, 1985] :

$$\frac{hD}{k} = Nu_D = 3.66 + \frac{0.0668Gz}{1 + 0.04Gz^{2/3}}, \tag{14}$$

where $Gz = Re\,Pr\,(D/L)$ is the Graetz number, $Re = (4\rho V/\pi D\mu)$ is the Reynolds number, $Pr = \mu/\rho k_a$ is the Prandtl number, L and D are the length and diameter of the segment, and $\dot{V}$ is the volumetric flow rate through the pipe. Using assumption 3, the bulk temperatures in and out of the section are equal to either T_h or T_c. The temperature difference ΔT then in (13) is approximated with $T_h - T_c$.

Furthermore, the heat flux can be expressed as a function of the inner film T_f and the outer wall temperature T_w as

$$\dot{q} = UA(T_w - T_f), \tag{15}$$

where U is the heat transfer coefficient through the combined metal wall, filter paper, and water film and is calculated as:

$$\frac{1}{U} = \frac{w}{k_{\text{st.steel}}} + R_s, \tag{16}$$

where, as in equation (11b),

$$R_s = \frac{1}{\frac{k_{water}}{\min(\delta, l)} + \frac{k_{paper}}{\min(\delta, l)} + \frac{\delta - \min(\delta, l)}{k_{water}} + \frac{l - \min(\delta, l)}{k_{paper}}}.$$

Equating equations (13) and (15) and solving for $(T_w - T_f)/(T_h - T_c)$ yield

$$\frac{T_w - T_f}{T_h - T_c} = h\left(\frac{w}{k_{st.steel}} + R_s\right). \quad (17)$$

The uncertainty could therefore be defined as

$$1 - \left(\frac{T_w - T_f}{T_h - T_c}\right) \times 100\%.$$

Equation (17) depends on the thickness of the materials and on the Reynolds number. The validity of assumption 3 decreases as *Re* increases but can be used in our analysis, since the instrument is operated usually at low *Re* and provides an upper limit estimate of the uncertainty. The appropriateness of assumption 3 can be assessed from the numerical solutions.

Figure 9 shows contours of $(T_w - T_f)/(T_h - T_c)$ as a function of water film and paper thickness. The wall thickness is assumed to be 1 cm, and the flow rate is equal to 10 L min^{-1}. As can be seen, the uncertainty is a somewhat strong function of filter paper thickness and has a weaker dependence on water film thickness. Everything else remaining constant, the minimum uncertainty is encountered when the water film and filter paper have the same thickness; under this condition the uncertainty ranges between 4 and 6%. However, when the water thickness becomes smaller than the filter paper (i.e., the paper partially dries), the magnitude of the uncertainty increases and can approach 10%, or higher. The reason for this behavior, which differs from the SDCC, lies in the fact that forced convection in the CCNS increases the heat transfer efficiency through the bulk of the fluid, and so the resistances in the water film and filter paper have a larger effect on the temperature drop across the wall than in the SDCC. Furthermore, the temperature differences between segments needed to generate supersaturations along the centerline are increased, compared with the SDCC; so the absolute value of the uncertainty increases along with it. For example, for $T_h - T_c = 10$ K, then, depending on the thickness of the water film, $T_w - T_f$ can range between 0.5 and 1 K.

Given that heat transfer efficiency increases with the flow rate, one would expect that $(T_w - T_f)/(T_h - T_c)$ depends on the flow rate. Indeed, this is the case, assuming that wall and paper thickness do not change, a tenfold increase in flow rate adds an additional 10% to the uncertainty; this would translate to a $T_w - T_f$ as high as 2 K if $T_h - T_c = 10$ K. As was stated before, assumption 3 is not as appropriate at high flow rates; so the uncertainty may not increase by as much as 10%, but still one would expect an appreciable change in film temperature.

In any case, especially when condensational heat flux is considered (which further increases the temperature uncer-

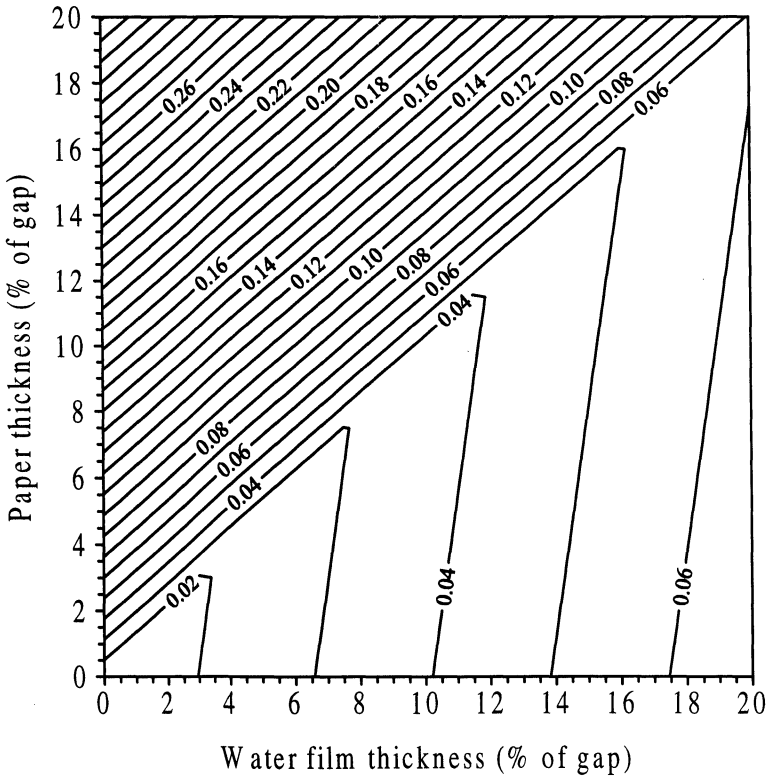

Figure 9. Contours of $(T_w - T_f)/(T_h - T_c)$ for the CCNS as a function of paper and water film thickness. The thickness of the metal wall is assumed to be 1 cm.

tainty), one would expect that the effective temperature in the instrument would be appreciably smaller than that posed on the walls. Therefore any simulations or experimental calibrations should be adjusted for this difference.

5.3. HCNS and FCNS Uncertainty Analysis

Both the HCNS and FCNS employ laminar flow between parallel plates. The two systems differ in the choice of the porous wetted layer; the FCNS uses filter paper (as in the SDCC and CCNS) while the HCNS uses porous metal. The thermal conductivity of the latter material is much higher than that of the paper, leading to much smaller temperature differences between the measured and surface temperatures. A general model that accounts for the resistance in the porous material will enable evaluation of the uncertainties in both systems.

In the following analysis, we assume as follows: (1) conditions are steady state; (2) one-dimensional conductive heat transfer is perpendicular to the flow, and convective heat transfer is along the flow axis; (3) the fluid reaches the developed linear temperature profile at the exit of each segment; (4) the sectional average temperature does not vary throughout the instrument (which is true in the HCNS for a symmetrically cold-hot temperature profile); (5) the flow field is fully developed and laminar; and (6) the latent heat flux owing to water condensation is small in comparison with the sensible heat transfer, which is reasonable for near-atmospheric pressures and small temperature differences. The geometry is defined in Figure 8c. Resistance through the steel matrix of the HCNS is neglected. With these assumptions, the problem reduces to a developing temperature profile in the entry region of an enclosed plate geometry, with the hydrodynamic flow field fully developed. Assumption 4 ensures that the bulk enthalpy of the fluid does not change as it passes through the instrument; thus any heat exchange between the plates is perpendicular to the flow. For a given segment, the heat flux through the hot wall, $\dot{q}^h$, can be expressed as a function of the inner film T_f^h and the outer wall temperature T_w^h as

$$\dot{q}^h = U^h A^h \left(T_w^h - T_f^h\right), \tag{18}$$

where U^h is the heat transfer coefficient through the combined metal wall, filter paper, and water film (equation (16)), and A^h is the exchange surface on the hot wall side. A similar expression can be written for the cold plate side:

$$\dot{q}^c = U^c A^c \left(T_w^c - T_f^c\right), \tag{19}$$

where T_f^c and T_w^c are the inner film and outer wall temperatures at the cold wall, respectively, and A^c is the exchange surface on the cold wall side. Furthermore, because the system is in steady state and the fluid does not experience any overall increase in enthalpy, $\dot{q}_h = \dot{q}_c$; so

$$U^h A^h \left(T_w^h - T_f^h\right) = U^c A^c \left(T_f^c - T_w^c\right). \tag{20}$$

Assuming that the surface areas and heat transfer coefficients are also equal, we get that

$$T_w^h - T_f^h = T_f^c - T_w^c, \tag{21}$$

which means that the temperature drop across the film is the same magnitude for both cold and hot walls. After further manipulations of equation (21) we obtain

$$\frac{T_f^h - T_f^c}{T_w^h - T_w^c} = 1 - 2\left(\frac{T_f^c - T_w^c}{T_w^h - T_w^c}\right). \tag{22}$$

The heat flux from the fluid to the cold film, $\dot{q}^c$, can also be expressed as

$$\dot{q}^c = hA^c \left(T_{\text{bulk}} - T_f^c\right), \tag{23}$$

where T_{bulk} is the bulk temperature of the fluid (which is the same along a segment) and h is the mean heat transfer coefficient. Since the system is in steady state, this heat flux is equal to the flux that passes through the cold wall (equation (19)). By equating the two fluxes and solving for T_f^c, we obtain

$$T_f^c = \frac{hT_{\text{bulk}} + U^c T_w^c}{h + U^c}. \tag{24}$$

By substituting equation (24) into equation (22), we finally get

$$\frac{T_f^h - T_f^c}{T_w^h - T_w^c} = 1 - 2\left(\frac{h}{h+U}\right)\left(\frac{T_{\text{bulk}} - T_w^c}{T_w^h - T_w^c}\right). \tag{25}$$

The uncertainty could therefore be defined as

$$\left(1 - \frac{T_f^h - T_f^c}{T_w^h - T_w^c}\right) \times 100\%.$$

The heat transfer coefficient h is calculated from equation (14) by using the hydraulic diameter. To incorporate the noncircular section effects, the heat transfer coefficient calculated from (14) is then multiplied by a factor of 2, which is the limiting factor for an aspect ratio approaching infinity [*Incropera and DeWitt,* 1985]. This approximation is reasonable, given that the HCNS examined here has an aspect ratio *W/H* = 20.

Equation (25) depends on the thickness of the materials and on the Reynolds number. However, if T_{bulk} remains the same between segments, then the uncertainty remains the same throughout the instrument. Given that heat transfer efficiency increases with the flow rate, one would expect that $(T_f^h - T_f^c)/(T_w^h - T_w^c)$ depends on the flow rate. Indeed this is the case, as shown by Figure 10. The wall thickness is 1.0 cm, and the paper thickness in this plot is assumed to be zero (therefore this plot shows the uncertainty for the HCNS). As can be seen, for a film thickness that is 5% of the gap, a tenfold increase in the flow rate almost doubles the uncertainty, from 11 to 18% (or a ratio of 0.89 to 0.82). However, for film thicknesses around 1% of the gap (or around 1 mm in our case), the flow rate has little effect on the uncertainty and remains around 3–5% (or a ratio of 0.97 to 0.95). For example, for $T_w^h - T_w^c = 5$ K, depending on the thickness of the water film, $T_f^h - T_f^c$ can range between 4.85 and 4.75 K, or the uncertainty is at most 0.25 K. Thus the temperature uncertainty is expected to have a minor effect on the instrument performance and is therefore neglected.

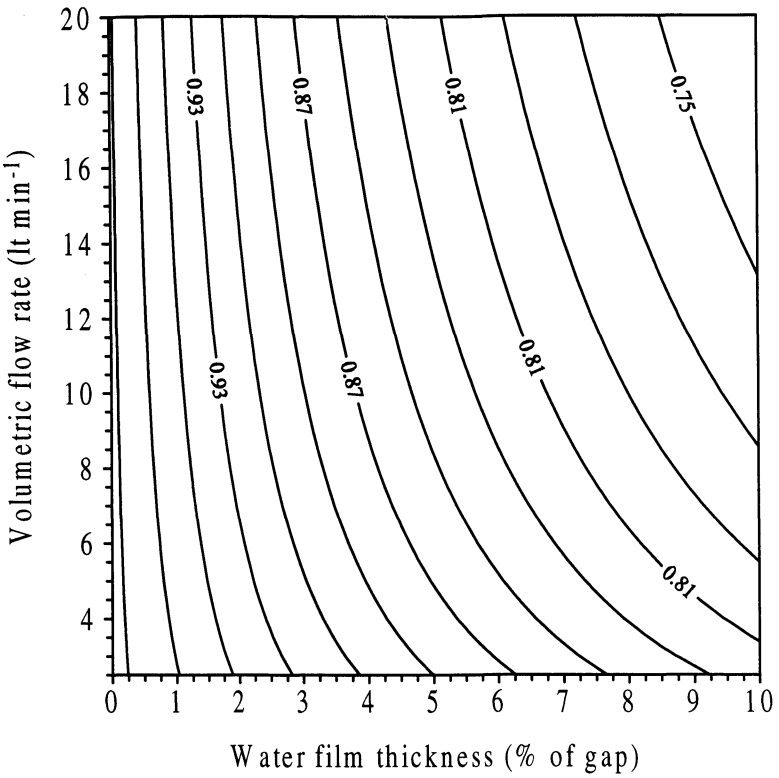

Figure 10. Contours of $(T_w - T_f)/(T_h - T_c)$ for the HCNS as a function of flow rate and water film thickness. The thickness of the metal wall is assumed to be 1 cm, and no filter paper is used.

The presence of the filter paper in the FCNS is expected to increase the temperature uncertainty, relative to the HCNS. For a paper thickness of 1 mm, which is well wetted, and wall thickness of 1 cm, the uncertainty is around 5%. A tenfold increase in the flow rate almost doubles the uncertainty, from 5 to 9% (or 0.95 to 0.91 ratio). For example, for $T_w^h - T_w^c = 5$ K, depending on the thickness of the water film, $T_f^h - T_f^c$ can range between 4.75 and 4.55 K, or the uncertainty ranges between 0.25 and 0.45 K. Thus although the uncertainty is increased with respect to the HCNS, it is still small enough to be considered minor.

6. Operating Conditions

After assessing the uncertainty in the wall temperature boundary condition for each device, the geometric dimensions, operating conditions, and aerosol used for simulating the performance of the instruments need to be specified. The dimensions and operating conditions of each instrument, which are summarized in Tables 2 to 5, are those reported in the literature. The SDCC dimensions were taken from an existing instrument (P. Chuang, internal communication, California Institute of Technology, 1999). The FCNS, HCNS, and

Table 2. Operating Conditions and Parameters for the SDCC (P. Chang, internal communication, 1999)

Parameter	Value/Range
Distance between plates, m	1×10^{-2}
Radius of plates, m	0.1
Thickness of view volume, m	1×10^{-3}
Radius of view volume, m	1×10^{-3}
Initial pressure, Pa	1.013×10^5
Initial relative humidity, %	100
Bottom plate temperature (constant), K	290
Top plate temperature (variable), K	292 to 297
Sidewall thickness, m	2×10^{-3}
Thermal conductivity of sidewall, W m^{-2} K^{-1}	1.4 (Plexiglas)
Ambient temperature, K	290

Table 3. Operating Conditions and Parameters for the FCNS [*Fukuta and Saxena*, 1979]

Parameter	Value/Range
Length, width, and height, m	0.838, 0.191, 0.018
Orientation	vertical
Distance from entrance where wall becomes wet on top and bottom plates, m	0.168, 0.168
Inlet pressure, Pa	1.013×10^5
Inlet relative humidity, %	100
Volumetric flow rate, $m^3 s^{-1}$	1.6667×10^{-4}
Inlet temperature (constant), K	283
Cold tip temperature (constant), K	283
Hot tip temperature (variable), K	284 to 293
Ambient temperature, K	290

CCNS dimensions were on the basis of those given in the literature [*Fukuta and Saxena*, 1979; *Hudson et al.*, 1981; *Hudson*, 1989, *Yum and Hudson*, 2000; *Chuang et al.*, 2000]. The dimensions used for the HCNS simulations [*Yum and Hudson*, 2000] are different from those reported by [1989] and reflect changes in the instrument that improve its resolution. Flow rates and wall temperatures are allowed to vary but, again, reflect reported operating conditions.

To determine the behavior of the instrument, we simulate the response of each instrument as a function of initial particle diameter; the inlet aerosol in all the simulations presented is assumed to be monodisperse and composed of ammonium sulfate. The number concentration in each instrument is assumed to be low, in order to minimize their effect on the supersaturation and temperature fields from the depletion of gas phase water vapor. This is particularly important for the SDCC, since biases in the supersaturation and temperature fields from the presence of the aerosol complicate growth history.

7. Simulation of Instrument Performance

7.1. SDCC

First, it is useful to determine the extent of wall effects, the time needed to attain the steady state profiles, and the concentration below which depletion effects (in the water vapor and temperature fields) are negligible. Simulations reveal that wall effects extend inward of the order of the gap between the plates, which covers roughly one seventh of the total radius. Thus wall effects are not expected to influence measurements made near the center of the instrument. The maximum concentration of the aerosol within the instrument, before depletion effects are seen, depends on both S_c and S_{max}; simulations indicate that concentrations below 1000 cm^{-3} inside the SDCC ensure that the supersaturation field is uninfluenced by the aerosol. When depletion effects are not important, the time needed to achieve steady state ranges between 3 s (for 7-K difference) to 5 s (for 2-K difference). An interesting feature is that the supersaturation profiles approach the steady state in a

Table 4. Operating Conditions and Parameters for the HCNS [*Hudson et al.*, 1981; *Hudson*, 1989; *Yum and Hudson*, 2000]

Parameter	Value/Range
Length, width, height, m	0.38, 0.3, 0.015
Height of aerosol injector	0.0015
Length of wetted wall on hot and cold side, m	0.28, 0.38
Total number of heated segments	9
Insulator length, m	0.001
Orientation	vertical
Sheath/aerosol volumetric flow ratio	10 to 20
Total volumetric flow rate, $m^3 s^{-1}$	3.3×10^{-4} to 5.0×10^{-5}
Inlet pressure, Pa	3.09×10^4
Aerosol, sheath flow inlet temperature (constant), K	295, 295
Aerosol, sheath flow inlet relative humidity, %	100, 90
Minimum cold side temperature, K	295–289
Maximum hot side temperature, K	295–301

Table 5. Operating Conditions and Parameters for the CCNS [*Chuang et al.*, 2000]

Parameter	Value/Range
Length, radius of tube, m	0.7, 9.27×10^{-3}
Radius of aerosol injector	2.29×10^{-3}
Total number of hot-cold pairs	7
Insulator length, m	0.01
Orientation of instrument	vertical
Sheath/aerosol volumetric flow ratio	0.7 to 20.0
Total volumetric flow rate, $m^3 s^{-1}$	1.166×10^{-5}
Inlet pressure, Pa	1.013×10^5
Inlet relative humidity, %	100
Aerosol, sheath flow inlet temperature (constant), K	295, 295
Aerosol, sheath flow inlet relative humidity, %	100, 90
a_T, a_C	1.0, 1.0 (case 1) 0.98, 0.041(cases 2-4)
Wall segment temperature profiles, K	295, 290, 295, 290, 295, 290, 295, 285, 295, 285, 295, 283, 295, 283 (case 1) 295, 290, 295, 290, 295, 290, 295, 285, 295, 285, 295, 283, 295, 283 (case 2) 294, 291, 294, 291, 294, 291, 294, 287, 294, 287, 294, 285, 297, 285 (case 3) 294, 292, 294, 292, 294, 292, 294, 289, 294, 289, 294, 287, 297, 287 (case 4)

nonsymmetric fashion, from the bottom plate to the top. Although the direction (from bottom to top or vice versa) could change (depending on the initial conditions in the instrument), the asymmetric approach to a steady state profile would tend to bias the particles on one side of the view volume toward larger sizes. The strength of this bias depends on the duration of the transients relative to the total growth time.

Plate 2a presents the simulated effective radius (defined as the third moment over the second moment of the droplet size distribution) within the view volume as a function of time for different dry aerosol sizes. Plate 3a represents the normalized aerosol concentration in the view volume as a function of time. In both plots, the initial aerosol concentration is uniform, and the temperature difference between the plates is kept at 2 K. This temperature difference generates a maximum supersaturation of about 0.15%. Under these conditions, particles with dry diameter larger than 0.1 μm should activate. Indeed, this is what is seen. Simulations for 0.05- and 0.09-μm particles yield constant effective radius and concentration, meaning that the particles grow to their equilibrium size, which is not large enough to experience significant sedimentation on the timescale of the simulations. Larger particles do show variability, and they are the ones that activate. The behavior of particles with a dry diameter of 0.50 μm differs from those of the other sizes examined, because sedimentation velocity of such particles is appreciable even for subsaturated conditions. As a result, the concentration in the view volume increases because aerosol from above falls through it more rapidly than the aerosol within the view volume falls out. The concentration of particles of smaller initial size stays relatively constant, as particles that fall out of the view volume are replaced by those from above. This behavior lasts roughly around 7 s, during which the slope of the effective radius curve is approximately the same for all particle sizes. After most of the aerosol above the view volume has passed through, the aerosol concentration starts dropping.

The behavior of the SDCC depends on the supersaturation profile, which can be characterized by the maximum supersaturation, S_{max}, and the critical supersaturation of the observed particles. Particles with $S_c \approx S_{max}$ activate only midway between the plates and are observed as they grow and sediment out of that small region. Their growth rate is initially slow; so concentration peaks late. On the other hand, particles with $S_c << S_{max}$ grow throughout much of the volume of the SDCC and relatively rapidly. Particles that activate well above the view volume grow and reach larger sizes as they sediment toward that level. The peak in r_{eff} for 0.05-μm particles occurs as much as 5 s later (not shown) than that for 0.5-μm particles. This large variation may account for the multiple peaks in scattered light intensity profiles seen when polydisperse aerosols are sampled.

Increasing the temperature difference between the plates increases S_{max}. A larger range of particle sizes satisfies the condition $S_c << S_{max}$, and the particle size dependence of the effective radius decreases as illustrated in Plates 2b and 3b, which are the same as Plates 2a and 3a, but for $\Delta T = 7$ K ($S_{max} = 1.81\%$). All of the particle sizes considered activate throughout half of the SDCC volume. Both the effective radius and droplet concentration in the view volume display similar time dependence over the 0.05- to 0.5-μm size range.

In determining the precision of the droplet diameter attained in the view volume, we define the "droplet diameter resolution," $R_{D_p} = D_p/\Delta D_p$, as the ratio of the mean diameter over its variation. A value of $R_{D_p} = 10$ means that the droplet diameter ranges around 10% of its mean value. A high value of this resolution throughout the duration of the measurement ensures that particles with the same critical supersaturation produce droplets that are close to being monodisperse within the view volume. Plate 4 displays R_{D_p} as a function of time, for various particle sizes. Plate 4a assumes a temperature difference between plates of 2 K, while Plate 4b is for a difference of 7 K. Because initially the aerosol in the SDCC is per-

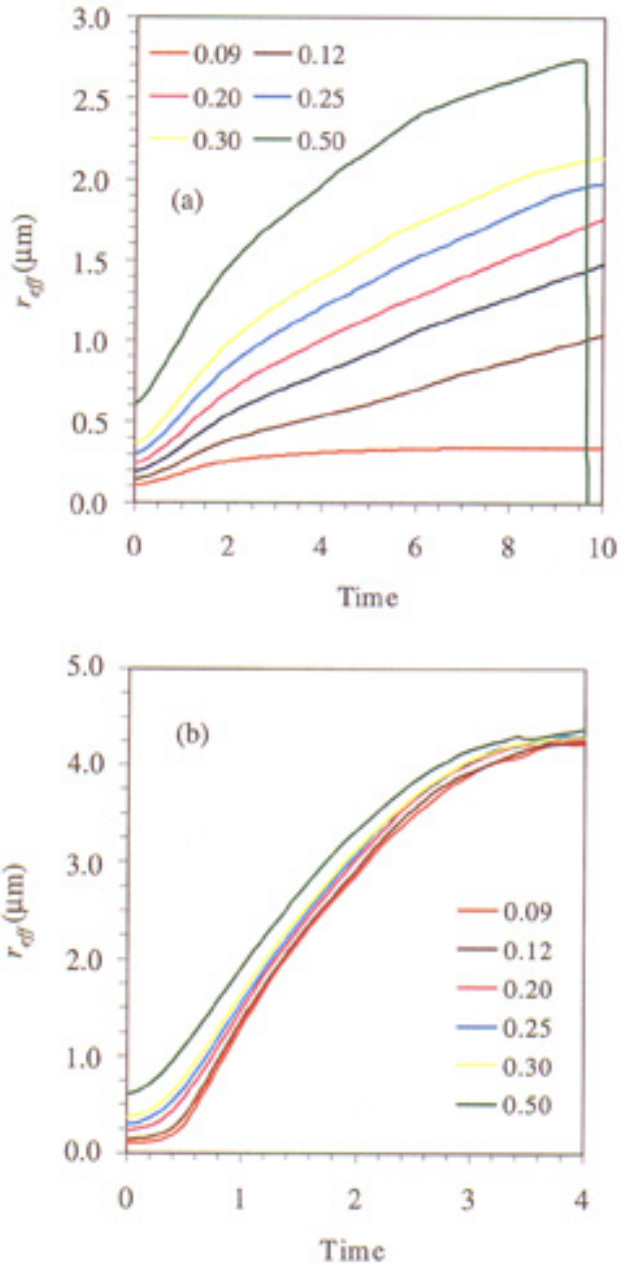

Plate 2. Simulated effective radius in the SDCC view window as a function of time for various initial particles sizes (dry diameter, micrometers). The temperature difference between the two plates is assumed to be (a) 2 K (S_{max} = 0.15%) and (b) 7 K (S_{max} = 1.81%).

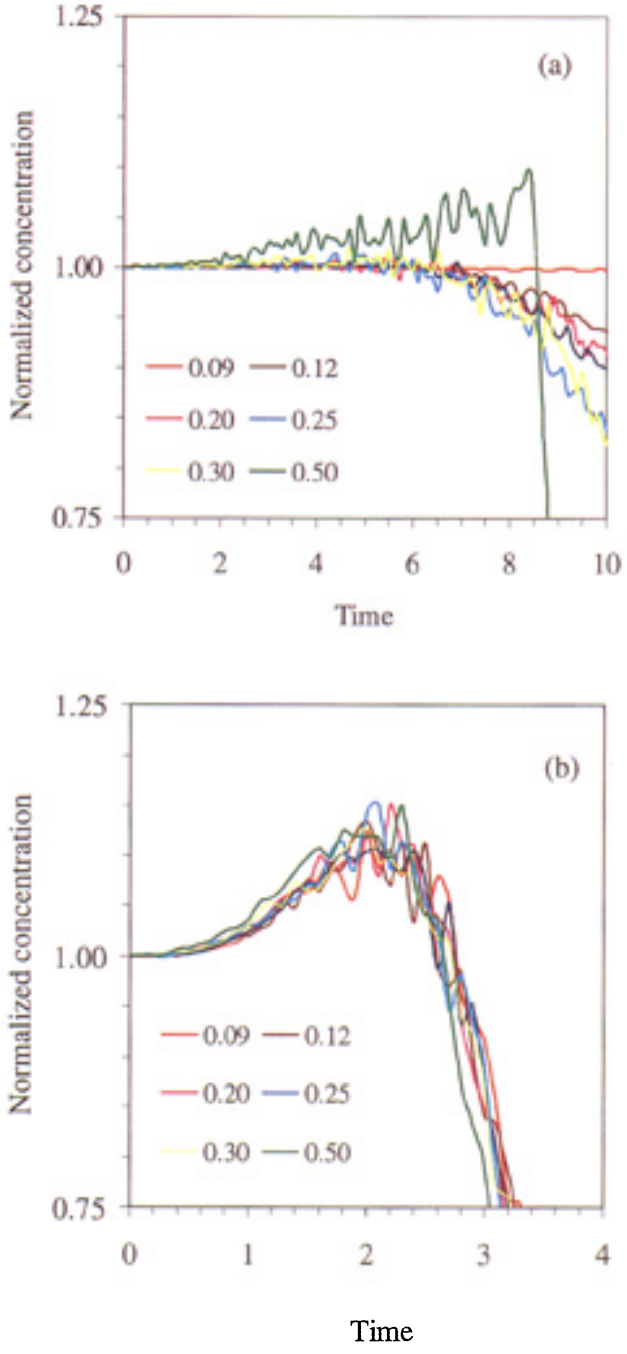

Plate 3. Simulated particle concentration in the SDCC view window as a function of time for various initial particles sizes (dry diameter, micrometers). The temperature difference between the two plates is assumed to be (a) 2 K (S_{max} = 0.15%) and (b) 7 K (S_{max} = 1.81%).

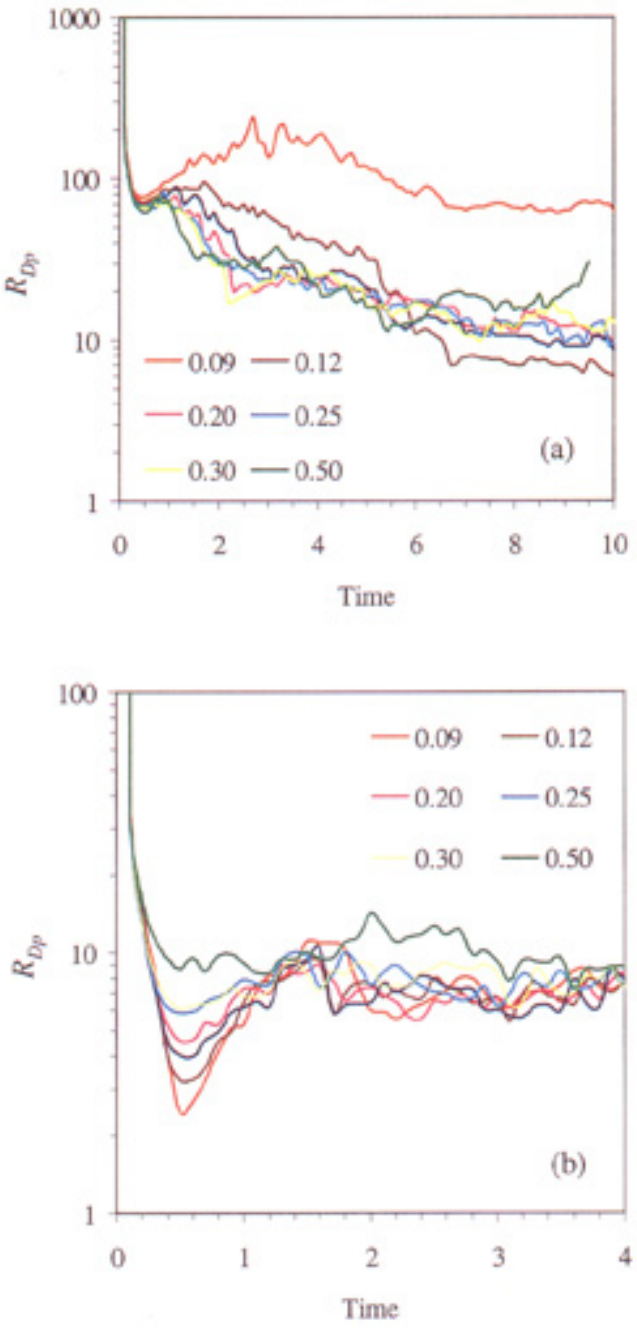

Plate 4. Simulated particle size resolution in the SDCC view window as a function of time for various initial particles sizes (dry diameter, micrometers). The temperature difference between the two plates is assumed to be (a) 2 K (S_{max} = 0.15%) and (b) 7 K (S_{max} = 1.81%).

fectly monodisperse, the resolution in both plots starts off from infinity. As the supersaturation profiles develop and the particles grow, R_{D_p} drops and fluctuates around the value of 10; this means that the droplet sizes range within 10% of their mean diameter, regardless of temperature difference or initial particle size (Table 6).

7.2. FCNS

The continuous flow in the FCNS eliminates some of the limitations that arise from the transient nature of SDCC measurements. However, buoyancy forces develop that limit the maximum temperature difference that can be imposed at a given flow rate. Simulations indicate that the maximum temperature difference that can be imposed for the reported flow rate is about 6 K, a value that agrees with the experimentally reported difference [*Fukuta and Saxena*, 1979]. Larger temperature differences lead to flow reversal. The simulations are relatively insensitive to the specific type of inlet velocity profile; so the results presented apply to both inlet velocity types.

The supersaturation fields that develop within the instrument control the growth of aerosol particles. Although the maximum value of the supersaturation can be estimated from the local temperature difference between the hot and cold walls and Figure 2, the supersaturation profile has to develop first before this maximum value is attained. Plate 5 shows supersaturation profiles for different streamlines along the centerline of the FCNS. As can be seen, half (or more) of the flow path is subsaturated, exposing particles to the maximum supersaturation for only a fraction of their residence time in the instrument. Moreover, the time in the supersaturated region decreases with decreasing S_{max}. Therefore particles with low S_c may not have sufficient time to activate by the time they reach the outlet. This difficulty is compounded by slow growth once activated at low S_{max}.

Buoyancy effects on the velocity field tend to distort the supersaturation profiles from being symmetric around the centerline; this deviation becomes stronger as the temperature difference between the plates increases. The position of the maximum supersaturation is also shifted slightly. Further away from the tips, the temperature gradient between the walls decreases, buoyancy effects become less important, and symmetric supersaturation (and temperature) profiles are attained. The centerline region, however, particularly for the low S_c streamlines, is relatively unaffected by buoyancy.

Plate 6 shows the simulated response curves for the FCNS. The horizontal axis represents the critical supersaturation of the inlet aerosol, and the vertical axis is the outlet wet diameter of the aerosol. Each curve represents a different centerline streamline with its own supersaturation. The particle outlet diameter is relatively insensitive to the inlet aerosol size, for particles for which $S_c < S_{max}$. Particles of $S_c > S_{max}$ do not activate; so there is a dramatic decrease in outlet size. The resulting "elbow" in the curve enables detection of particles with $S_c < S_{max}$ of the specific streamline, since there is a clear distinction between particles that activate and those that do not. The sharper this "elbow" is, the better resolved the CCN concentration is at the given supersaturation. Farther away from the heated tips, the maximum supersaturation decreases, and the position of the "elbow" shifts toward lower critical supersaturations. However, because growth at lower supersaturations is slower and because the particle exposure to the maximum supersaturation is briefer, droplets do not grow as much (in comparison with larger supersaturation streamlines). As a consequence, the elbow becomes less pronounced, eventually vanishing completely. The elbow more or less disappears at S_c = 0.1%, in agreement with the value reported by *Fukuta and Saxena* [1979]. In its current configuration, the FCNS can probe effectively CCN with S_c between 0.1 and 1.0%.

7.3. CCNS

At first glance, this instrument seems to avoid many of the problems encountered in the FCNS. Buoyancy effects are not

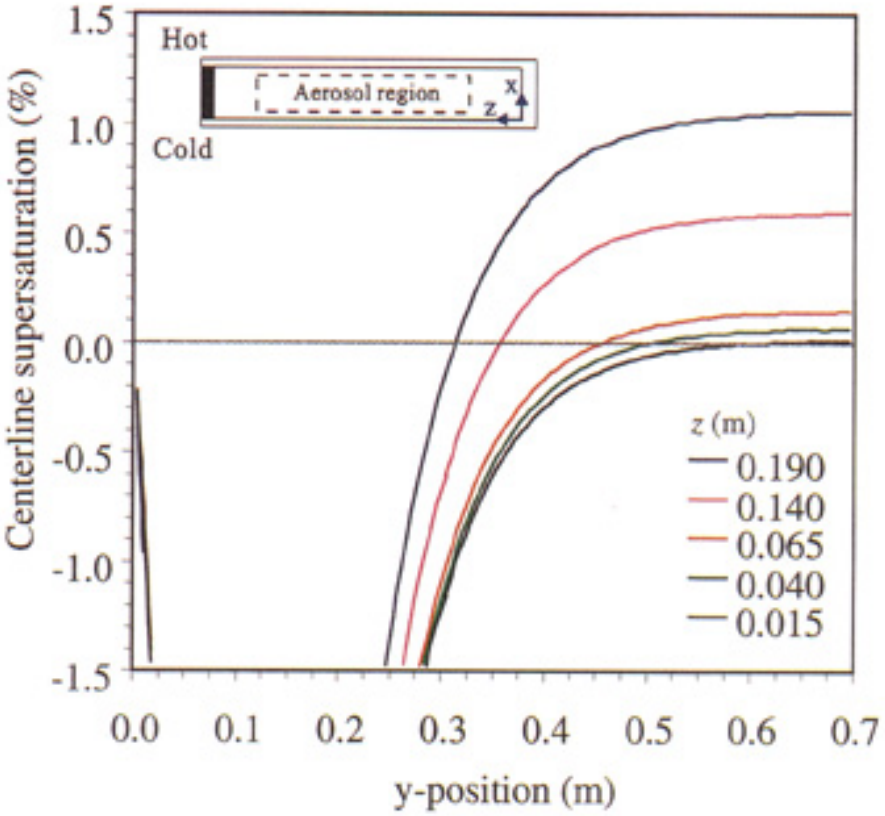

Plate 5. Supersaturation (percent) profiles for different streamlines along the centerline of the FCNS.

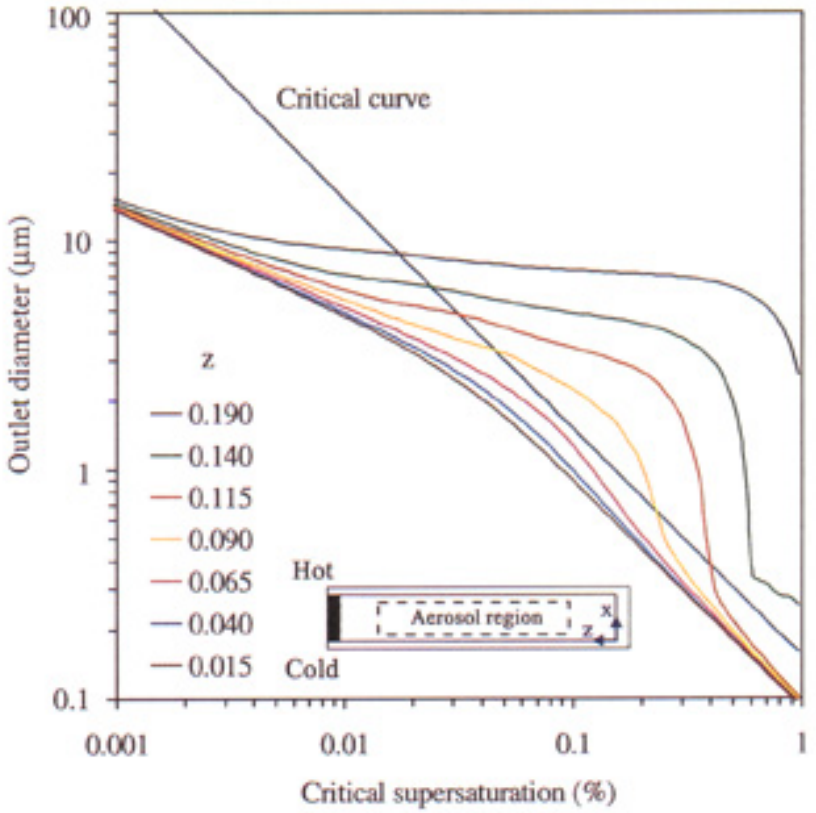

Plate 6. Simulated growth curves for selected streamlines of the FCNS. The temperature difference between the tips is 5 K, and the volumetric flow rate is 20 L min^{-1}.

Table 6. Summary of SDCC Simulations

ΔT, K	S_{max}, %	Dry Diameter of Smallest $(NH_4)_2SO_4$ Particle Activated, μm	$D_p/\Delta D_p$ in View Volume		
			Mean	Minimum	Maximum
2	0.15	0.101	14.8	12.6	21.0
3	0.34	0.059	10.0	8.3	13.7
4	0.60	0.040	10.2	5.0	12.7
5	0.93	0.030	8.9	4.0	11.4
6	1.34	0.024	9.3	0.2	13.4
7	1.81	0.019	10.5	8.7	13.0

significant, and most of the instrument is utilized for exposing the particles to supersaturations (Figure 7). The supersaturation profile is, however, considerably more complex, making it more difficult to assess instrument behavior on the basis of the temperature and supersaturation profiles alone. It is, therefore important to evaluate the sensitivity of the predicted outlet droplet distribution to the parameters that affect particle growth. Two very important parameters affecting the simulations are the film temperature at the wall (which determines the supersaturation) and the mass accommodation coefficient (which affects the particle growth).

Figure 11 shows predicted and measured calibration curves for the CCNS. Details about the experimental data can be found in the work of *Chuang et al.* [2000]. Curves corresponding to cases 1 to 4 in Figure 11 represent the temperature boundary conditions and accommodation coefficients specified in Table 5. Case 1 represents an accommodation coefficient of unity and the nominal wall temperatures as the wall boundary conditions. The predicted size is larger (by about a factor of 2) than the measured data. When lowering the temperature boundary condition by around 2–3 K (which, according to section 5.2, is a reasonable drop, especially since latent heat flux through the film can further increase the uncertainty), the predicted curves (case 3, case 4) lie close to the experimental data. Changing the accommodation coefficient from 1.0 to 0.041 further improves the predictions. In all cases, though, the qualitative behavior of the curve does not change: the outlet diameter of droplets is relatively insensitive to critical supersaturation (particularly when the droplets are activated). Thus the model captures the essential features of the instrument despite the complex growth behavior imposed by the supersaturation profile that develops in the instrument. For subsequent simulations, case 3 conditions are used.

From both simulations and experimental data, it is clear that the droplet size at the outlet of the CCNS is relatively insensitive to the initial particle size. For a range of critical su-

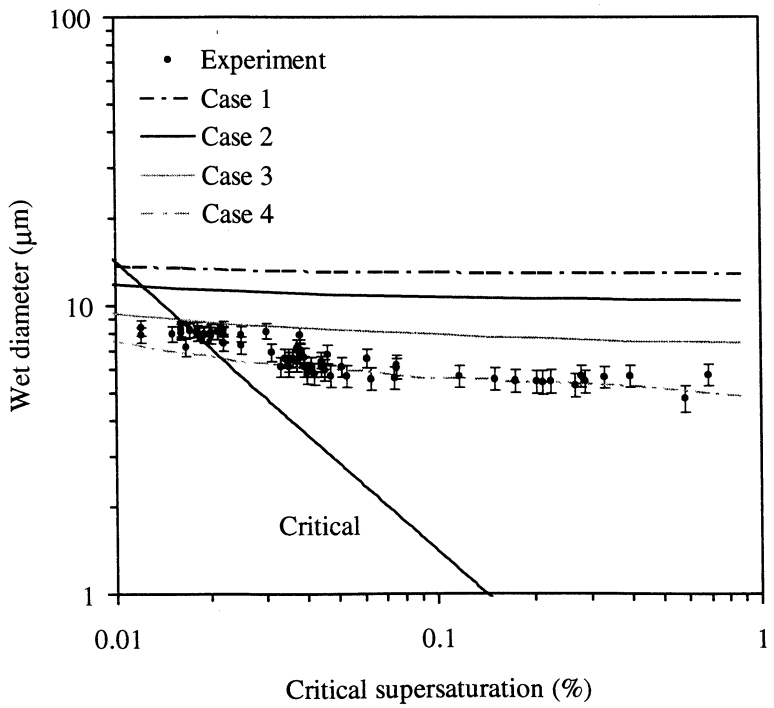

Figure 11. Experimental and simulated calibration curves for the CCNS. The different simulation cases correspond to different values of effective wall temperature and accommodation coefficients, the values of which are given in Table 5.

persaturation spanning 2 orders of magnitude, the outlet diameter changes at most by a factor of 2. This low sensitivity arises from the particle growth kinetics. At the late stages of growth, when the particle is in the continuum size region and solute and surface tension effects are minor, equation (1) can be integrated to yield

$$D_p^2 = D_{po}^2 + \frac{\int_{t_{act}}^{t} S_v dt}{\frac{\rho_w RT}{4p^* D_v M_w} + \frac{\Delta H_{vap}\rho_w}{4k_a T}\left(\frac{\Delta H_{vap} M_w}{TR} - 1\right)}. \quad (26)$$

The particle size at activation, D_{po}, is relatively small; so at sufficiently long growth time,

$$D_p^2 \approx \frac{\int_{t_{act}}^{t} S_v dt}{\frac{\rho_w RT}{4p^* D_v M_w} + \frac{\Delta H_{vap}\rho_w}{4k_a T}\left(\frac{\Delta H_{vap} M_w}{TR} - 1\right)}, \quad (27)$$

i.e., all particles approach the same size, regardless of initial size (or S_c). This asymptotic approach of all particles to the same size also explains the uniform response of the SDCC for $S_c << S_{max}$ and the consistent final particle size of the FCNS over a wide range of supersaturations.

Despite the weak dependence of outlet diameter on particle critical supersaturation, the simulations can be used to compute the resolution in measured droplet diameter necessary for resolving the CCN spectrum. Since the aerosol occupies a finite region of the flow field, not all particles are exposed to the same supersaturation or have the same residence time. As a consequence, a monodisperse inlet aerosol will produce a droplet distribution with finite spread; this effect may interfere with the ability to resolve a CCN spectrum, since droplets of a given size at the outlet are not unambiguously related to critical supersaturation. This spread at the outlet is a function of the sheath to aerosol flow rate ratio (because that determines the uniformity of the supersaturation field and residence time to which the particles are exposed) and will decrease with increasing ratio.

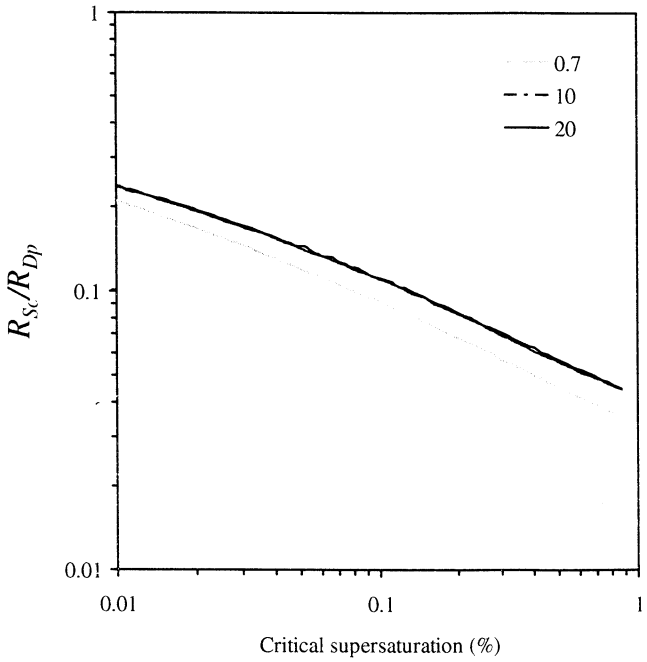

Figure 12. Predicted resolution ratio R_{S_c}/R_{D_p} for the CCNS, for different values of $\dot{V}_{sheath}/\dot{V}_{aerosol}$. The case 3 (Table 5) values of effective wall temperature and accommodation coefficients are used.

In determining the precision of the droplet diameter measurement needed, we use the droplet diameter resolution, R_{D_p}, and the critical supersaturation resolution, $R_{S_c} = S_c/\Delta S_c$. Dividing these two quantities, we get the "resolution ratio," R_{S_c}/R_{D_p}, which can then be related to the instrument response:

$$\frac{R_{S_c}}{R_{D_p}} = \frac{S_c}{D_p}\frac{\Delta D_p}{\Delta S_c} \approx \frac{S_c}{D_p}\left[\frac{dD_p}{dS_c}\right]_{cc}, \quad (28)$$

where $[dD_p/dS_c]_{cc}$ is the slope of the calibration curve at the given S_c. Figure 12 displays the resolution ratio computed for the CCNS for different sheath to aerosol flow rate ratios. Figure 12 illustrates that the resolution in critical supersaturation is between 10 and 100 times smaller than the droplet diameter resolution for the volumetric flow rate ratio used in the calibration experiment. This means that if the diameter measurement has an uncertainty of 1% (or $R_{D_p} = 100$), the uncertainty in critical supersaturation will range between 10 and 100%. Increasing the flow rate ratio increases the resolution notably, but only up to a certain extent; the difference in resolution between ratios of 10 and 20 is quite minimal. This is understandable because the aerosol at such a high flow rate ratio occupies a volume very close to the centerline; so the particles are exposed essentially to a uniform supersaturation profile. The resolution ratio is also a strong function of S_c: it varies almost by a factor of 10 for S_c, ranging between 0.01 and 1%. This is a result of the change in the calibration curve slope, which approaches zero as S_c increases; this means that for particles of high S_c, droplet size is more or less insensitive to S_c or that the asymptotic limit of equation (27) has practically been reached. This is not true for activated particles with low S_c; the D_{po} term in equation (26) is not negligible, and outlet particle size still varies with S_c.

To estimate the uncertainty in critical supersaturation from the spread induced by the instrument, we use equation (28), and obtain that

$$\frac{\Delta S_c}{S_c} = \frac{1}{R_{S_c}} \approx \frac{|\Delta D_p|_{inst}}{S_c}\left[\frac{dD_p}{dS_c}\right]_{cc}^{-1}, \quad (29)$$

where $\Delta S_c/S_c$ is the supersaturation uncertainty and $|\Delta D_p|_{inst}$ is the variation in droplet diameter, calculated from the instrument model. Figure 13 displays $\Delta S_c/S_c$ as a function of supersaturation, for the CCNS. The uncertainty was predicted by using the curves of Figure 12 and the variability of the calculated outlet droplet diameter. As can be seen, the resulting uncertainty is large, ranging from 100 to over 1000%. This is expected, since the relative variation in droplet diameter at the

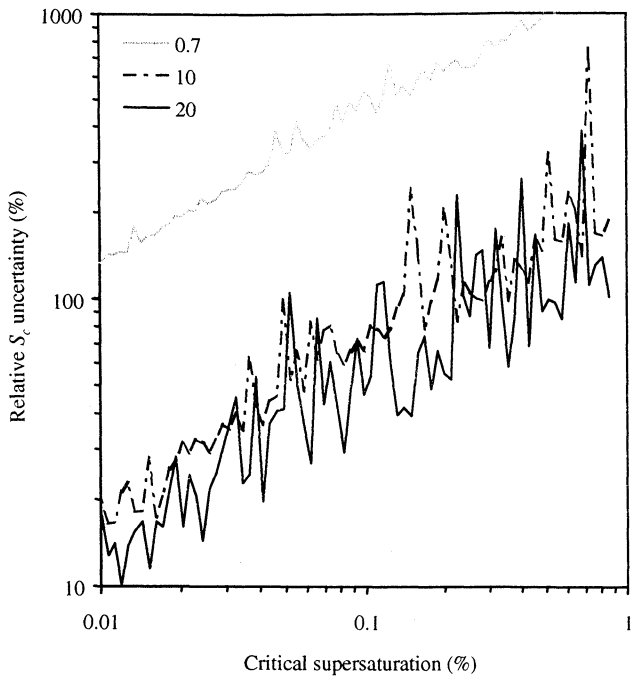

Figure 13. Relative critical supersaturation uncertainty as a function of critical supersaturation, for the CCNS. Each curve represents different values of $\dot{V}_{sheath}/\dot{V}_{aerosol}$. The uncertainty was predicted by using the curves of Figure 12, and the variability of the outlet droplet diameter (calculated by the model results).

CCNS outlet is, on average, between 15 and 20% (Table 7). Therefore the aerosol/sheath flow rate ratio used for the operation of this instrument is very influential for obtaining a CCN spectrum. While increasing this ratio to 10 or 20 considerably reduces the uncertainty, the uncertainty still exceeds 50% for $S_c > 0.04\%$. Further increasing the flow ratio might decrease the uncertainty, but obtaining good droplet counting statistics then becomes a problem.

7.4. HCNS

The HCNS exposes particles to supersaturation profiles that vary smoothly and monotonically in the streamwise direction. Simulations were performed for several different temperature profiles at low (6 L min^{-1}) and high (20 L min^{-1}) total volumetric flow rates (Plates 7a and 7b, respectively). The sheath to aerosol flow ratio was assumed to be 10. These simulations reveal that the droplet growth kinetics, like those for the CCNS, lead to a restricted range of final droplet size for particles with a wide range of critical supersaturations. For example, when the maximum plate temperature is set to more than 6 K, the outlet droplet diameter changes by a factor of 2 for critical supersaturations that span 2 orders of magnitude (between 0.01 and 1%). This variation does not seem to be strongly influenced by the volumetric flow rate (although the outlet droplet diameter is) but depends strongly on the temperature profile in the instrument. Improvement is seen only when the maximum temperature difference drops to 4 K; in this case, the variation in droplet diameter increases considerably but has the drawback that particles with $S_c > 0.4\%$ do not activate. As can be seen, the resolution of the instrument increases as the outlet droplet size gets closer to the critical curve; the drawback to this is that the S_c range for which particles are activated becomes more restricted.

Calibration data available in the literature [*Yum and Hudson*, 2000] do not precisely specify the maximum temperature difference (or the total volumetric flow rate) used in the HCNS, making it difficult to precisely assess the performance of the HCNS model. In addition, the data provide the mean channel number (as opposed to particle diameter) as a function of critical supersaturation. However, since mean channel number scales linearly with particle size, the nondimensionalized mean channel number and mean particle diameter are equivalent quantities:

$$\frac{F(S_c) - F(S_{c,\text{high}})}{F(S_{c,\text{low}}) - F(S_{c,\text{high}})} = \frac{D_p(S_c) - D_p(S_{c,\text{high}})}{D_p(S_{c,\text{low}}) - D_p(S_{c,\text{high}})},$$

where F is the mean channel corresponding to critical supersaturation S_c. Using these non-dimensionalized quantities, we compare measurements to the model predictions (Plate 8). As can be seen, the measurements are very close to model predictions for a volumetric flow rate of 20 L min^{-1} and a maximum temperature difference of 6 K. Given that these values of flow rates and maximum temperature difference are within reported operating conditions, we can assume that the model captures the behavior of the HCNS.

Plate 9 displays the predicted resolution ratio, R_S/R_{D_p}, for the HCNS, for different temperature profiles and total volumetric flow rates of: (Plate 9a) 6 L min^{-1}, and (Plate 9b) 20 L min^{-1}. The sheath to aerosol flow ratio was assumed to be 10. Here the instrument sensitivity is increased in relation to that of the CCNS, particularly for low temperature differences and critical supersaturations between 0.1 and 1%. For a maximum

Table 7. Predicted Outlet Droplet Diameter Variability and Resulting Critical Supersaturation Uncertainty for the CCNS (Critical Supersaturation Range Between 0.01 and 1.0%)

$\frac{\dot{V}_{sheath}}{\dot{V}_{aerosol}}$	$\frac{\Delta D_p}{D_p}$, %			$\frac{\Delta S_c}{S_c}$, %		
	Mean	Minimum	Maximum	Mean	Minimum	Maximum
0.7	28.9	9.7	57.4	303.0	25.1	1326.2
10.0	5.5	1.1	36.5	53.7	2.7	755.3
20.0	4.0	0.6	19.3	38.6	1.5	388.3

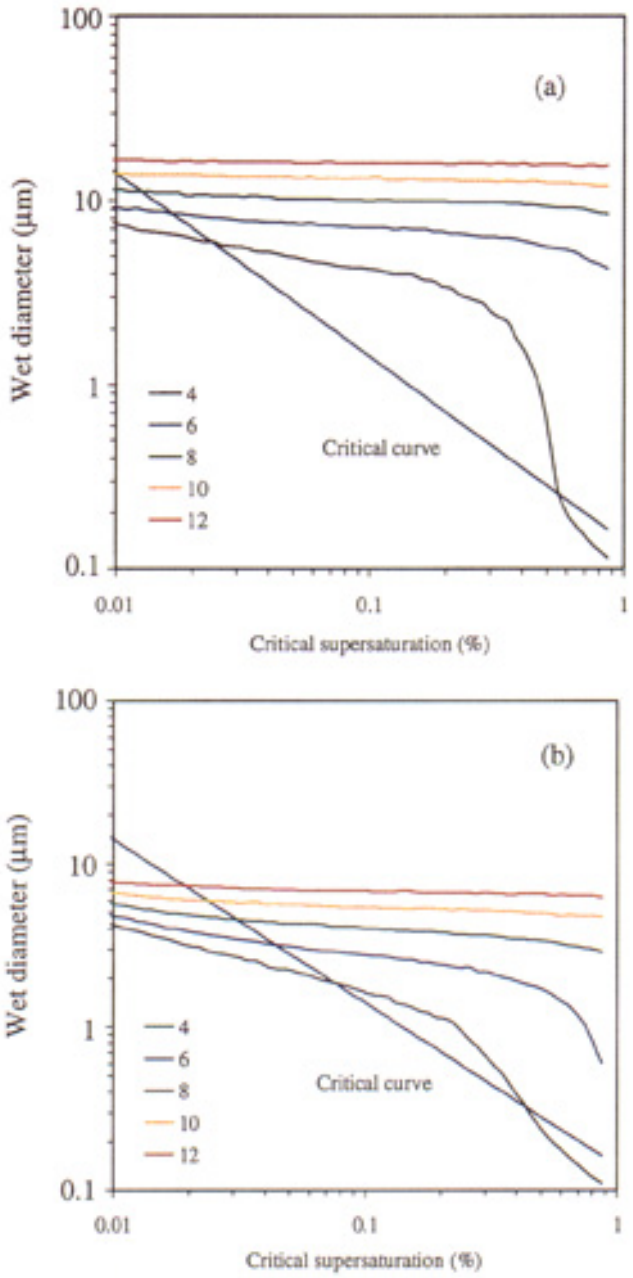

Plate 7. Simulated calibration curves for the HCNS, for various maximum temperature differences, ΔT_{max} (the ΔT at the last segment), and a volumetric flow rate of (a) 6 L min^{-1} and (b) 20 L min^{-1}. The temperature difference between each segment is assumed to increase with a constant step ("linear ramp") on both cold and warm sides.

temperature difference of 4 and 6 K, the resolution increases dramatically for $S_c > 0.1\%$. This happens because the supersaturation generated in these cases is not sufficient to activate particles with S_c close to 1%; so an "elbow" similar to those in Plate 6 develops. Consequently, the calibration curve slope becomes much steeper around the region of this elbow. Because of this, it is expected that the uncertainty in the critical supersaturation is considerably lower than that for the CCNS. Indeed, this is the case, as is shown by Plate 10. The uncertainty was computed by using equation (28) and the calculated variability of the outlet droplet diameter. Plate 10a refers to a volumetric flow rate of 6 L min^{-1}, and Plate 10b has a flow rate of 20 L min^{-1} (sheath to aerosol ratio is 10). For these conditions, the relative variation in droplet diameter at the HCNS outlet is on average only between 2 and 3% (Table 8). However, this is enough to generate substantial uncertainty in S_c. Minor fluctuations in this variability account for the large fluctuations seen in the computed uncertainty. For example, for a maximum temperature difference of 8 K (which is an operational value reported by *Hudson* [1989]), the S_c uncertainty ranges between 30 and 100% and can reach as high as 390%. When the maximum temperature difference is around 4 K, the resolution improves by an order of magnitude and averages around 10%. The simulations indicate that a spectrum can be obtained for critical supersaturations between 0.08 and 0.8%. Particles outside of this range do not activate, either because the supersaturation is lower than the critical value or simply because there are kinetic limitations that inhibit low-supersaturation particles from activating.

Compared with the CCNS, the HCNS seems to exhibit less uncertainty; this is attributed to the smoother and monotonic supersaturation profiles generated in the HCNS. The oscillations in the flow direction seen for CCNS slow down (or even reverse) particle growth; so less of the instrument is utilized for particle growth. Because of this, particles of different critical supersaturations essentially grow to the same size by the time they reach the outlet of the instrument.

8. Summary and Conclusions

The behavior and performance of four cloud condensation nucleus instruments are theoretically analyzed. These include the static diffusion cloud chamber (SDCC), the Fukuta continuous flow spectrometer (FCNS), the Hudson continuous flow spectrometer (HCNS), and the Caltech continuous flow spectrometer (CCNS). A numerical model of each instrument on the basis of reported instrument dimensions and operating conditions is constructed on the basis of a general fluid dynamics code coupled to a description of aerosol growth/activation microphysics. Instrument performance is explored by simulating instrument response to a monodisperse ammonium sulfate aerosol. The CCNS and HCNS models were compared with experimental measurements and found to be in good agreement. The FCNS model predictions agreed with instrument limitations reported in the literature.

Uncertainties in the wall temperature boundary condition vary with instrument construction and arise mainly from the presence of filter paper (used for wetting instrument walls). Using a simple heat transfer model for each instrument, this uncertainty is found to be negligible for the SDCC (of the order of 0.01 K) and very small for the HCNS and FCNS (ranging between 0.25 and 0.45 K). It can be appreciable for the CCNS (ranging between 0.5 and 2 K); so the wall boundary condition in the instrument simulations must be adjusted to account for this. The numerical model for the CCNS reproduces experimental measurements, when the wall temperature boundary conditions is adjusted by a factor slightly higher than that predicted by this simple uncertainty analysis.

SDCC exhibit the least uncertainty in the wall temperature boundary conditions and produce droplets that are (for a given critical supersaturation) monodisperse to within 10% of the droplet diameter, throughout the duration of the measurement. The FCNS is an instrument that can be used as a CCN spec-

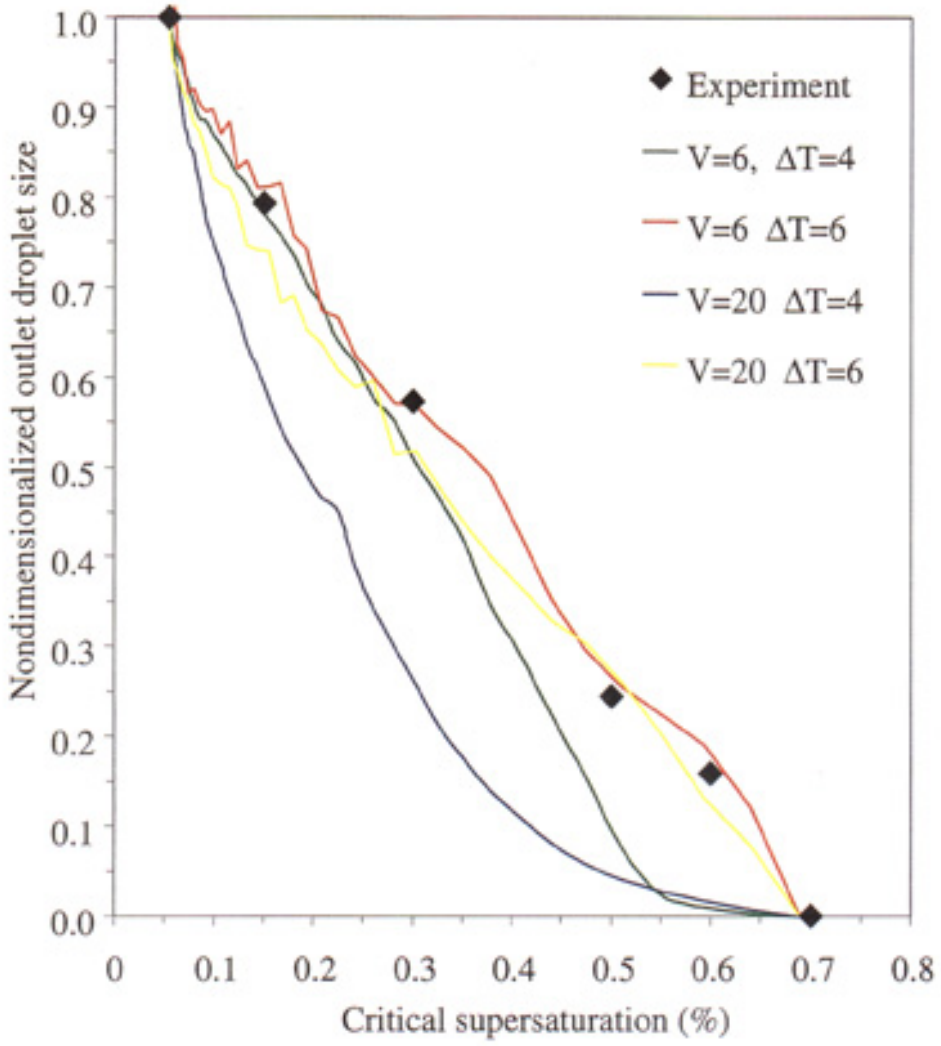

Plate 8. Experimental and simulated calibration curves for the HCNS. Non-dimensionalized droplet diameter is plotted as a function of critical supersaturation. V is the total volumetric flow rate, and ΔT is the maximum temperature difference between the plates. $\dot{V}_{sheath}/\dot{V}_{aerosol} = 10$ in the simulations.

Table 8. Predicted Outlet Droplet Diameter Variability and Resulting Critical Supersaturation Uncertainty for the HCNS ($\dot{V}_{sheath}/\dot{V}_{aerosol} = 10$, Critical Supersaturation Range Between 0.01 and 1.0%)

Maximum ΔT, K	$\dot{V}$, L min^{-1}	$\frac{\Delta D_p}{D_p}$, %			$\frac{\Delta S_c}{S_c}$, %		
		Mean	Minimum	Maximum	Mean	Minimum	Maximum
4	6	2.6	0.5	9.0	14.1	1.2	30.9
6	6	2.7	0.6	8.6	35.5	7.5	67.2
8	6	3.2	0.5	9.2	102.5	15.8	393.2
10	6	3.6	0.6	12.8	163.2	16.0	670.2
12	6	3.0	0.4	10.1	203.8	20.2	723.8
4	20	2.4	0.6	10.0	11.4	0.9	26.3
6	20	2.8	0.4	8.8	22.4	7.3	47.9
8	20	3.1	0.4	7.4	31.5	5.6	61.6
10	20	2.6	0.5	7.2	76.7	14.2	259.6
12	20	3.2	0.3	11.6	108.3	7.8	423.4

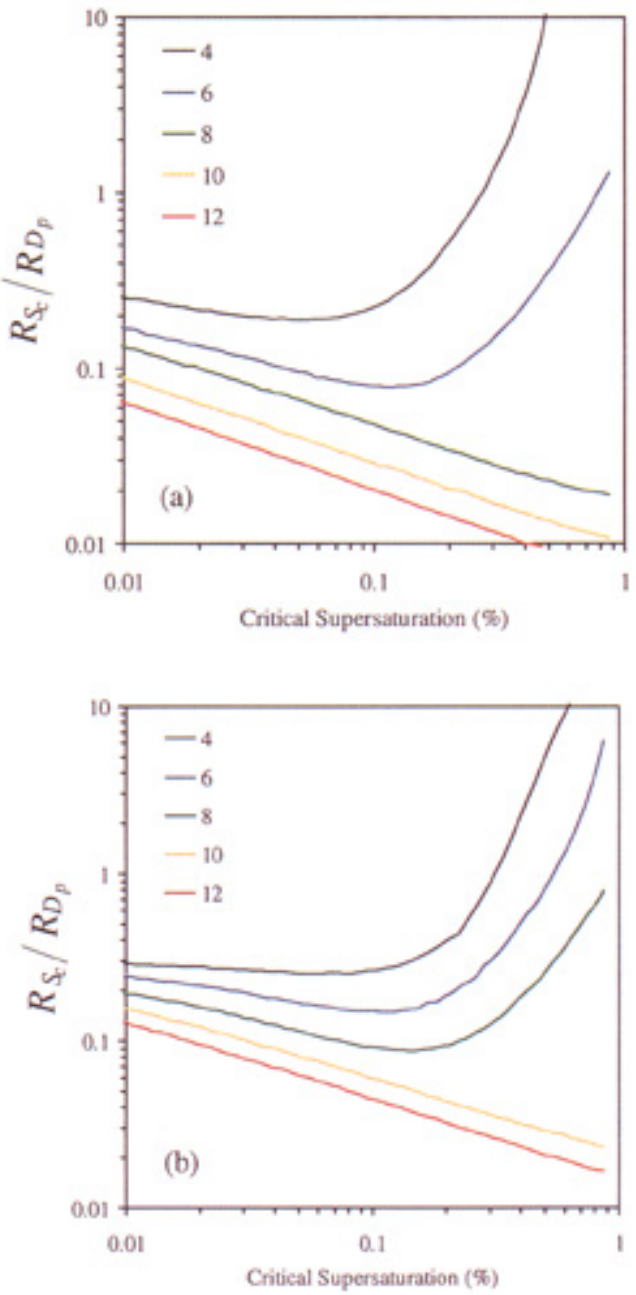

Plate 9. Predicted resolution ratio R_{S_c}/R_{D_p} for the HCNS, for different ΔT_{max}, and a volumetric flow rate of (a) 6 L min^{-1} and (b) 20 L min^{-1}. $\dot{V}_{sheath}/\dot{V}_{aerosol} = 10$ in these simulations.

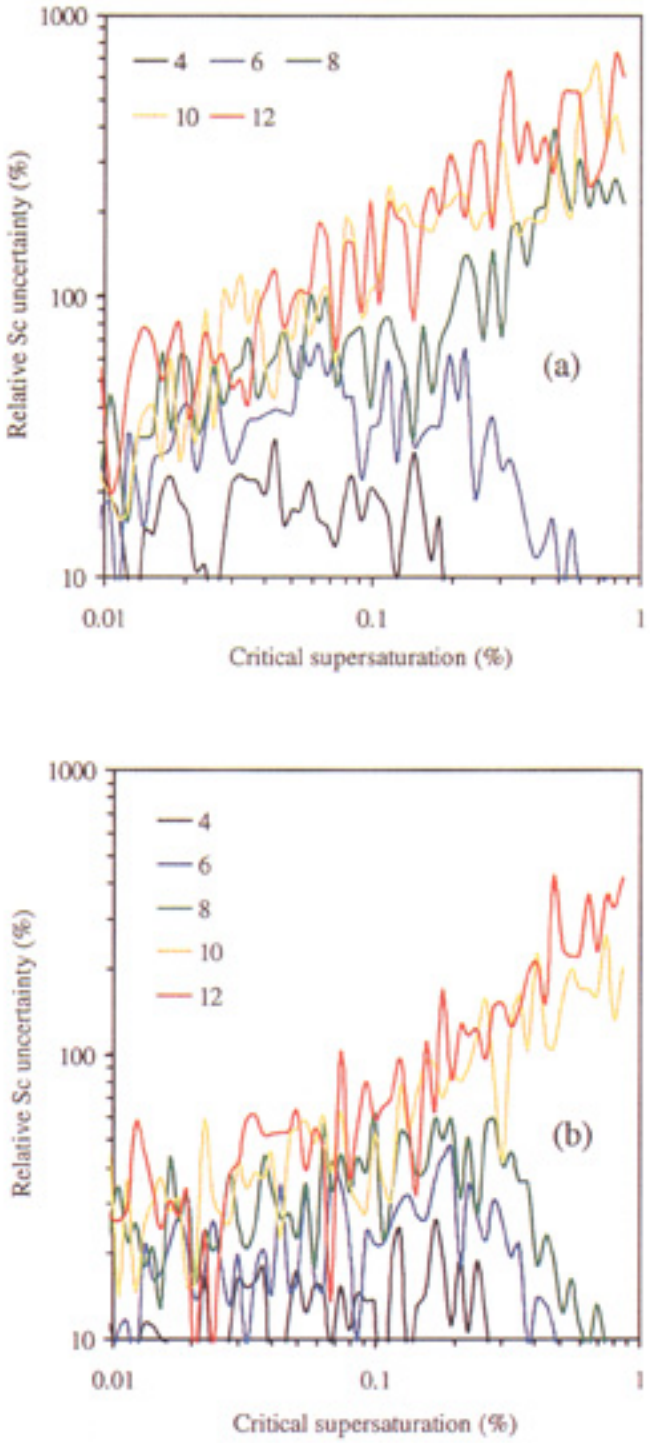

Plate 10. Relative critical supersaturation uncertainty as a function of critical supersaturation, for the HCNS. The uncertainty was predicted by using the curves of Plate 9 and the variability of the outlet droplet diameter (calculated by the model results). Volumetric flow rates of (a) 6 L min^{-1} and (b) 20 L min^{-1}. $\dot{V}_{sheath}/\dot{V}_{aerosol} = 10$ in these simulations.

trometer, since different streamlines attain different supersaturations, allowing particles to activate over a range of critical supersaturations. The range of critical supersaturations that can be measured is limited because (1) the temperature difference must be kept small enough to avoid buoyancy-induced flow reversal or secondary flows and (2) the instrument loses its sensitivity for particles of critical supersaturation lower than 0.1% because the particles do not have enough time for growth. The first issue is not a serious limitation, since the supersaturation on the high temperature difference side is sufficiently high to include all the climatically important aerosol. The second limitation, however, constrains the ability to probe the climatically critical low supersaturation CCN. Both HCNS and CCNS have inherent limitations in the ability to resolve the distribution of particles with respect to critical supersaturation. The most important parameters affecting the performance of dynamic spectrometers are the maximum temperature difference between the walls, the total volumetric flow rate, and the sheath to aerosol volumetric flow ratio. For the monodisperse ammonium sulfate aerosol considered here, conditions can be found for the HCNS for which an activation spectrum can be resolved for critical supersaturations between 0.08 and 0.8%. Simulations for the HCNS indicate that the calculated uncertainty in critical supersaturation exceeds 100% when the maximum temperature difference exceeds 6 K for 20 L min^{-1} total flow rate or 8 K for 6 L min^{-1} total flow. The same uncertainty can decrease to 10% (on average) when the temperature difference is reduced to 4 K. The uncertainty, however, is not uniform and depends strongly on the initial size of the particle. The predicted uncertainty in the critical supersaturation for the CCNS is on average above 50%.

While different design parameters or operating conditions may lead to modest shifts in the performance from that predicted for any of the four instruments, the essential features described in this paper are inherent to their designs.

Notation

A heat exchange area.
a_c condensation coefficient.
a_T thermal accommodation coefficient.
C water vapor concentration, moles per cubic meter.
C_p specific heat of controlled-temperature wall.
c_p specific heat of dry air at constant pressure.
C_c slip correction factor.
d_p particle dry diameter.
D_v water vapor diffusivity in air.
D_v' water vapor diffusivity in air, corrected for noncontinuum effects.
D_p particle wet diameter.
F mean channel number in particle size measurement of HCNS.
g acceleration of gravity.
h heat transfer coefficient.
H instrument height.
J_{buoy} momentum generated by thermal buoyancy.
J_{cond} rate of liquid water condensation on aerosol particles.
k_a thermal conductivity of air.
k_a' thermal conductivity of air, corrected for noncontinuum effects.
k_{paper} thermal conductivity of filter paper.
$k_{st.steel}$ thermal conductivity of stainless steel.
k_{wall} thermal conductivity of wall.
k_{wat} thermal conductivity of liquid water.
l paper thickness.
L instrument length.
M_a molecular weight of dry air.
M_w molecular weight of water.
n number of size sections in aerosol distribution.
n_s number of moles of solute per particle.
N aerosol number concentration.
P air pressure.
Pr Prandtl number.
p_v water vapor pressure.
p_v^* saturation vapor pressure of water.
$\dot{q}$ heat flux.
r radial coordinate.
R universal gas constant.
Ra Rayleigh number.
R_{D_p} droplet diameter resolution, $D_p/\Delta D_p$.
Re Reynolds number.
R_{S_c} critical supersaturation resolution, $S_c/\Delta S_c$.
R_s thermal resistance through the soaked filter paper.
s wall coordinate of FCNS instrument.
S_c critical supersaturation for activation, according to Köhler equilibrium theory.
S_{max} maximum supersaturation.
S_v supersaturation.
S_v^{eq} supersaturation in equilibrium with particle size.
t time.
T_w average temperature of SDCC wall.
T temperature.
T_{bulk} section average (bulk) temperature.
$\dot{V}$ volumetric flow rate.
u_t terminal velocity.
u velocity component.
U heat transfer coefficient.
v velocity component.
w wall thickness.
W instrument width.
w_L liquid water content (kilogram of liquid water per volume of air).
x_1, x_2 generalized spatial coordinates.
x, y Cartesian coordinates.
z axial coordinate.

ΔH_{vap} enthalpy of evaporation of water.
δ water film thickness.
λ mean free path of air.
μ air viscosity.
ν_s number of ions the solute dissociates into in solution.
ρ density of air.
ρ_p density of particle.
ρ_w density of water.
σ_w water surface tension.

Subscripts-superscripts

amb ambient.
f film.
c cold wall.
h hot wall.
w wall.
t top wall.
b bottom wall.

Acknowledgments. This work was supported by Office of Naval Research grant N00014-91-0119. We would also like to acknowledge Timothy VanReken for performing part of the CCNS calibration curve experiments.

References

Alofs, D. J., Performance of a dual-range cloud nucleus counter, *J. Appl. Meteorol., 17,* 1286–1297, 1978.

Chuang, P. Y., A. Nenes, J. N. Smith, R. C. Flagan, and J. H. Seinfeld, Design of a CCN instrument for airborne measurement, *J. Atmos. Oceanic Technol., 17,* 1005-1019, 2000.

Fukuta, N., and V. K. Saxena, A horizontal thermal gradient cloud condensation nucleus spectrometer, *J. Appl. Meteorol., 18,* 1352–1362, 1979.

Fukuta, N., and L. A. Walter, Kinetics of hydrometer growth from the vapor; spherical model, *J. Atmos. Sci., 27,* 1160-1172, 1970.

Gosman, A. D., and A. Ideriah, TEACH-2E, *Tech. Rep. FM-83-2,* Univ. of Calif., Berkeley, 1976.

Hindmarsh, A. C., ODEPACK: A systematized collection of ODE solvers, in *Scientific Computing,* edited by R. S. Stepleman et al., pp. 55-64, North-Holland, New York, 1983.

Hoppel, W. A., S. Twomey, and T. A. Wojciechowski, A segmented thermal diffusion chamber for continuous measurements of CN, *J. Aerosol Sci., 10,* 369-373, 1979.

Hudson, J. G., An instantaneous CCN spectrometer, *J. Atmos. Oceanic Technol., 6,* 1055–1065, 1989.

Hudson, J. G., C. F. Rogers, and G. Keyser, Simultaneous operation of three CCN counters and an isothermal haze chamber at the 1980 International CCN Workshop, *J. Rech. Atmos., 15,* 271-283, 1981.

Incropera F. P, and D. P. DeWitt, *Fundamentals of Heat and Mass Transfer,* John Wiley, New York, 1985.

Laktionov, A. G., A constant-temperature method of determining the concentrations of cloud condensation nuclei, *Izv. Acadsci. USSR Atmos. Oceanic Phys.,* Engl. Transl., *8,* 672–677, 1972.

Lala, G. G., and J. E. Jiusto, An automatic light scattering CCN counter, *J. Appl. Meteorol., 16,* 413–418, 1977.

McMurry, P. H., A review of atmospheric aerosol measurements, *Atmos. Environ., 34,* 1959-1999, 2000.

Patankar, S. V., *Numerical Heat Transfer and Fluid Flow,* McGraw-Hill, New York, 1980.

Seinfeld, J. H., and S. N. Pandis, *Atmospheric Chemistry and Physics,* John Wiley, New York, 1998.

Shulman, M. L., M. C. Jacobson, R. J. Charlson, R. E. Synovec, and T. E. Young, Dissolution behavior and surface tension effects of organic compounds in nucleating cloud droplets, *Geophys. Res. Lett., 23,* 277–280, 1996.

Sinnarwalla, A. M., and D. J. Alofs, A cloud nucleus counter with long available growth time, *J. Appl. Meteorol., 12,* 831–835, 1973.

Twomey, S., Measurements of natural cloud nuclei, *J. Rech. Atmos., 1,* 101–105, 1963.

Yum, S. S., and J. G. Hudson, Vertical distributions of cloud condensation nuclei spectra over the springtime Arctic Ocean, *J. Geophys. Res.,* in press, 2000.

P. Y. Chuang, National Center for Atmospheric Research, Boulder, CO 80307. (chuang@ucar.edu)

R. C. Flagan, A. Nenes, and J. H. Seinfeld, California Institute of Technology, Pasadena, CA 91125. (flagan@its.caltech.edu; nenes @its.caltech.edu; and seinfeld@its.caltech.edu

(Received March 16, 2000; revised September 13, 2000; accepted September 21, 2000.)